Author/s:
Mackintosh, V;Kohn, B;Gleadow, A;Tian, Y

Title:
Phanerozoic Morphotectonic Evolution of the Zimbabwe Craton: Unexpected Outcomes From a Multiple Low-Temperature Thermochronology Study

Date:
2017-10-01

Citation:
Mackintosh, V., Kohn, B., Gleadow, A. & Tian, Y. (2017). Phanerozoic Morphotectonic Evolution of the Zimbabwe Craton: Unexpected Outcomes From a Multiple Low-Temperature Thermochronology Study. Tectonics, 36 (10), pp.2044-2067. https://doi.org/10.1002/2017TC004703.

Persistent Link:
https://hdl.handle.net/11343/293528

Mackintosh Vhairi (Orcid ID: 0000-0003-4545-2038)
Kohn Barry (Orcid ID: 0000-0001-5064-5454)
Gleadow Andrew (Orcid ID: 0000-0003-0496-0028)
Tian Yuntao (Orcid ID: 0000-0001-5480-9962)

Phanerozoic morphotectonic evolution of the Zimbabwe Craton: unexpected outcomes from a multiple low-temperature thermochronology study

Vhairi Mackintosh[1], Barry Kohn[1], Andrew Gleadow[1], and Yuntao Tian[2]

[1]School of Earth Sciences, University of Melbourne, Melbourne, Victoria, 3010, Australia

[2]School of Earth Sciences and Engineering, Sun Yat-sen University, Guangzhou, 510275, China

Corresponding author: Vhairi Mackintosh (vmackintosh@student.unimelb.edu.au)

Key Points:

- Zimbabwe Craton experienced uplift and denudation following stress transmission from Pan-African orogenesis during Gondwana amalgamation
- First zircon He data reveal removal of variable km-scale Karoo sedimentary cratonic cover began in the Paleogene
- Zircon He ages younger than apatite He or fission track ages suggest moderate eU zircons can be ultra-low-temperature thermochronometers

This is the author manuscript accepted for publication and has undergone full peer review but has not been through the copyediting, typesetting, pagination and proofreading process, which may lead to differences between this version and the Version of Record. Please cite this article as doi: 10.1002/2017TC004703

Abstract

The fragmentary Phanerozoic geological record of the anomalously elevated Zimbabwe Craton makes reconstructing its history difficult using conventional field methods. Here, we constrain the cryptic Phanerozoic evolution of the Zimbabwe Craton using a spatially extensive apatite (U-Th-Sm)/He (AHe), apatite fission track (AFT) and zircon (U-Th)/He (ZHe) dataset. Joint thermal history modelling reveals that the region experienced two cooling episodes inferred to be the denudational response to surface uplift. The first and most significant protracted denudation period was triggered by stress transmission from the adjacent ~750-500 Ma Pan-African orogenesis during the amalgamation of Gondwana. The spatial extent of this rejuvenation signature, encompassing the current broad topographic high, could indicate the possible longevity of an ancient topographic feature. The ZHe data reveal a second, minor denudation phase which began in the Paleogene and removed a km-scale Karoo cover from the craton. Within our dataset, the majority of ZHe ages are younger than their corresponding AHe and AFT ages, even at relatively low eU. This unexpectedly recurrent age 'inversion' suggests that in certain environments, moderately, as well as extremely, damaged zircons have the potential to act as ultra-low-temperature thermochronometers. Thermal history modelling results reveal that the zircon radiation damage accumulation and annealing model (ZRDAAM) frequently over-predicts the ZHe age. However, the opposite is true for extremely damaged zircons where the ZHe and AHe data are also seemingly incompatible. This suggests that modification of the ZRDAAM may be required for moderate to extreme damage levels.

1 Introduction

The fragmentary nature of the geological record of cratons makes reconstructing their Phanerozoic evolution difficult to elucidate using conventional field methods. In southern Africa, the Phanerozoic history of the cratonic regions is of particular interest because they are located at an average, enigmatic elevation of ~1000 m (Fig. 1a), compared to most other cratonic regions where average elevations are between ~400-500 m [*Lithgow-Bertelloni and Silver*, 1998]. The southern African topographic anomaly has generated great scientific interest and in turn controversy surrounding the cause [e.g. Lithgow-Bertelloni and Silver, 1998; Moore et al., 2009b; Molnar et al., 2015] and timing of this phase (or phases) of surface uplift [e.g. *Burke*, 1996; *Brown et al.*, 2002; *Doucouré and de Wit*, 2003; *Moore et al.*, 2009b; *Flowers and Schoene*, 2010; *Rudge et al.*, 2015]. The Zimbabwe Craton makes up the northeastern part of the anomalously elevated southern African plateau (Fig. 1a). The Phanerozoic history of the Zimbabwe Craton is particularly poorly constrained as the current exposure is dominated by pre-cratonization Archean granites and gneisses which also lack any structural controls (Fig. 2).

Low-temperature thermochronology (LTT) studies of basement rocks have provided an invaluable tool for deciphering the cryptic Phanerozoic histories of cratonic settings [e.g. *Lorencak et al.*, 2004; *Ault et al.*, 2009; *Flowers and Kelley*, 2011; *Wildman et al.*, 2017]. The strength of the LTT method lies in its ability to quantitatively constrain the timing and rates of processes that disrupt the thermal regime of the upper crust over geological timescales [e.g. *Reiners et al.*, 2005]**.** Moreover, when cooling signals can be attributed to denudation then the LTT data provide quantitative constraints on the spatial and temporal pattern of regional denudation and allow for a more thorough understanding of the long-term landscape evolution of cratons. As an array of thermal histories can generate similar LTT ages then the use of multiple thermochronometers on the same sample can constrain the range of plausible thermal histories and provide a more robust record of crustal cooling [e.g. *Flowers et al.*, 2015]. This is particularly true of systems with overlapping temperature sensitivities such as the apatite (U-Th-Sm)/He (AHe) (~30-90 °C) [*Flowers et al.*, 2009], the apatite fission track (AFT) (~60-120 °C) [*Wagner and Van den haute*, 1992] and potentially the zircon (U-Th)/He (ZHe) (~0-220 °C) system depending on the amount of accumulated radiation damage [*Guenthner et al.*, 2013].

Despite the extensive successful application of LTT studies in other regions of southern Africa, LTT studies of Zimbabwe are considerably lacking. Previous published work in southern Africa has largely focused on sampling across the Great Escarpment and passive continental margin of South Africa and Namibia with the dominantly AHe and AFT data revealing different aspects of its Mesozoic and Cenozoic evolution [*Brown et al.*, 1990, 2002, 2014; *Brown*, 1992; *Gallagher and Brown*, 1999; *Cockburn et al.*, 2000; *Raab et al.*, 2002, 2005; *Luft et al.*, 2005; *Tinker et al.*, 2008; *Kounov et al.*, 2008, 2009; *Flowers and Schoene*, 2010; *Wildman et al.*, 2015, 2016; *Green et al.*, 2015; Fig. 1a]. Very few studies have investigated the morphotectonic histories of the cratonic interior regions of southern African and the spatial coverage of those that have is limited [*Brown*, 1992; *Brown et al.*, 2002, 2014; *Raab et al.*, 2002; *Belton and Raab*, 2010; *Flowers and Schoene*, 2010; *Beucher et al.*, 2013; *Stanley et al.*, 2015; *Wildman et al.*, 2017; Fig. 1a]. This is significant because as shown by recent work [*Stanley et al.*, 2015; *Wildman et al.*, 2017], the cooling and denudation response to horizontal tectonic-derived stresses as well as vertical mantle-derived stresses of the cratonic interior can differ markedly to that of the off-craton (or cratonic margin) regions.

The sparse data currently available for the Zimbabwe Craton are limited mainly to the peripheral areas of the craton and are restricted to AFT data [*Noble*, 1997; *Belton*, 2006; *Belton and Raab*, 2010; Fig. 1b]. All AFT ages from the central cratonic interior, with the exception of one from the center of the craton, are generally old (>170 Ma) (Fig. 1b) with short mean track lengths (MTLs) indicative of a protracted slow cooling history through the AFT partial annealing zone (PAZ) (~60-120 °C) [*Wagner and Van den haute*, 1992]. Limited forward modelling of the northern Zimbabwe Craton suggests that the region cooled below ~120 °C in the Carboniferous and experienced slow protracted cooling through the PAZ until the Late Jurassic [*Noble*, 1997]. *Belton* [2006] similarly concluded that the central cratonic interior had resided close to the surface since the Jurassic. However, as illustrated in Figure 1b, these conclusions are based on AFT data from just five samples scattered across the cratonic interior.

Here, we present the first AHe and ZHe data, as well as a more spatially extensive AFT dataset (Fig. 1b), for the Zimbabwe Craton and this region of southern Africa. By using a multi-thermochronometer approach, we aim to unravel a significant portion of the unexplored Phanerozoic morphotectonic history of the Zimbabwe Craton.

2 Geological, tectonic and morphological setting

The Zimbabwe Craton makes up the core of Zimbabwe and is surrounded by late Archean to Early Cambrian mobile belts (Fig. 2). The craton is comprised of an Archean granite-gneiss-greenstone complex (Fig. 2) which formed during two main crustal growth events in the early (~3.8-3.2 Ga) and late (~3.0-2.6 Ga) Archean [Wilson et al., 1995]. The ~2.575 Ga Great Dyke [*Oberthur et al.*, 2002; Fig. 2], a mafic and ultramafic complex which intruded along NNE trending fractures, cuts across the craton and is undeformed. This suggests that stabilization of the Zimbabwe Craton occurred over ~25 Myr [Armstrong and Wilson, 2000].

The recorded post-cratonization history of the Zimbabwe Craton is highly fragmentary. Numerous kimberlite and carbonatite intrusions pierce the Zimbabwe Craton but only a few have been dated [*Jelsma et al.*, 2004, 2009; *Moore et al.*, 2012]: the ~538 Ma Sese [*Smith et al.*, 2004] and ~533 Ma Colossus [*Allsopp et al.*, 1985] kimberlites as well as the ~205 Ma Dorowa carbonatite [*Nicolaysen et al.*, 1962; *Jelsma et al.*, 2004] (Fig. 2). Most preserved evidence for Proterozoic and Phanerozoic activity in Zimbabwe is largely restricted to the surrounding mobile belts and margins of the craton (Fig. 2). The preserved Proterozoic record on the craton is restricted to the Paleoproterozoic to Mesoproterozoic metasediments of the Frontier Formation and overlying Umkondo Group [*Hanson et al.*, 1998; Fig. 2] as well as the emplacement of the ~1.88 Ga Mashonaland dolerite sill complex [*Campbell et al.*, 1991; *Söderlund et al.*, 2010; Fig. 2].

Geochronological evidence suggests that from the Late Proterozoic to Early Devonian (~550-400 Ma) the far eastern margin of the Zimbabwe Craton underwent thermal rejuvenation [*Vail*, 1966; *Manhica et al.*, 2001; *Grantham et al.*, 2011; *Chaúque et al.*, 2017]. The early rejuvenation signature is most likely associated with the broadly coincident Pan-African Kuunga Orogeny, which is used here to refer to the ~570-505 Ma Kuunga events of *Meert* [2002] and ~550-520 Ma Malagasy events of *Collins and Pisarevsky* [2005] following the broader nomenclature of *Fritz et al.* [2013]. The Kuunga Orogeny involved the fairly concurrent amalgamation of the Indian, East Antarctic, Australian, Kalahari (the Zimbabwe and Kaapvaal Cratons sutured by the Limpopo Belt) and Congo Cratons during the final stages of Gondwana assembly [e.g. *Meert*, 2002]. The collisions involved the formation of the Zambezi Belt to the north of the study area [e.g. *Vinyu et al.*, 1999; *Hargrove et al.*, 2003; *Itano et al.*, 2016; inset of Fig. 2] as well as deformation and metamorphism in the southern Mozambique Belt to the east of the study area [e.g. *Manhica et al.*, 2001; *Bingen et al.*, 2009; *Itano et al.*, 2016; inset of Fig. 2]. The later cratonic rejuvenation signal of the eastern margin could be broadly associated with a ~533-486 Ma post-orogenic extension and magmatic stage in the adjacent southern Mozambique Belt [*Jacobs et al.*, 2008; *Bingen et al.*, 2009; inset of Fig. 2]. However, the spatial extent to which the Zimbabwe Craton was affected by the Kuunga orogenesis and post-orogenic stage is poorly constrained.

The preserved Phanerozoic record of the Zimbabwe Craton is largely restricted to the west where strata of the Mid-Zambezi Karoo and Kalahari basins extend over the craton [*Johnson et al.*, 1996]. A few thin scattered outliers are preserved in the interior of the craton (Fig. 2) and could suggest a previously more extensive Phanerozoic sedimentary cover existed at one stage. The Mid-Zambezi Basin formed as a half-graben within the Magondi Belt (inset of Figure 2) and is composed of ~2000 m to over 4000 m of late Carboniferous to Early Jurassic sedimentary and igneous rocks of the Karoo Supergroup, which lie unconformably on Archean basement [*Orpen et al.*, 1989; *Johnson et al.*, 1996]. The Karoo sedimentary strata comprise a Lower Karoo sequence of glacial beds, mudstones and shales, and an Upper Karoo sequence of grits and sandstones which are separated by an unconformity of approximately Permian-Triassic boundary age [*Johnson et al.*, 1996]. The final Karoo event involved the emplacement of basaltic lava at ~179.2 ± 0.9 Ma in the Mid-Zambezi Basin [*Jones et al.*, 2001]. These Karoo basalts were part of the Karoo(-Ferrar) Large Igneous Province (LIP), which covered most of southern Africa and extended into Antarctica and Australia, and were emplaced when Zimbabwe was located centrally within Gondwana [*Duncan et al.*, 1997]. Extrusion of extensive Karoo basalts in the Early Jurassic followed closely and are thus suggestive of a causative link with the Early to Middle Jurassic (~180-165 Ma) separation of East Gondwana (Antarctica-India-Madagascar) and West Gondwana (Africa-South America) [e.g. *Veevers*, 2012].

The post-Karoo geological record of the craton comprises ~100 m of Late Jurassic to Cretaceous sandstones of the Gokwe Formation [*Barber*, 1993] that are preserved as scattered outcrops along the western region of the craton and ~100 m of the Kalahari Group (Fig. 2). Kalahari Basin sediments that extend over the craton are made up of variably consolidated calcareous and siliceous (Pipe) sandstones (with variable duricrust formation) capped by the unconsolidated, aeolian Kalahari Sands [*Thomas and Shaw*, 1990; Fig. 2]. The age of the sediments and formation of the Kalahari Basin is rather uncertain due to the lack of diagnostic fossils and difficulty in determining the nature of duricrust horizons and potentially redistributed sediments [*Thomas and Shaw*, 1988]. However, as Kalahari sediments overly Cretaceous sediments in the west of Zimbabwe, it is estimated that Kalahari sedimentation began in the Late Cretaceous/Paleogene and continued into the Quaternary [*Haddon and McCarthy*, 2005].

The current topography of the Zimbabwe Craton is dominated by a northeast-southwest trending low-relief, broad topographic high, rising from ~1400 m in the southwest to over 2300 m in the Eastern Highlands of Zimbabwe [*Lister*, 1987; Figs. 1a and 1b]. The axis of this broad topographic high makes up the current central watershed (Fig. 1b) and separates the three main drainage basins of Zimbabwe, namely the Zambezi Basin in the north and the Limpopo and Save basins in the south. The central watershed of Zimbabwe forms part of one of three main drainage divides in southern Africa that have been interpreted as axes of epeirogenic uplift [*Du Toit*, 1933; *Moore*, 1999].

3 Thermochronology methods, results and discussion

Eighteen bedrock samples from the Archean granitic-gneissic basement and one Triassic Karoo sandstone (96Z-16) were selected for this study due to their outcropping location within the broad topographic high forming the interior of the Zimbabwe Craton (Figs. 1b and 2). Full sample details can be found in Table S1. Apatite and zircon grains were separated using conventional mineral separation techniques including rock crushing, sieving, heavy liquid and magnetic separation.

3.1 Apatite fission track analysis

AFT thermochronology is based on the accumulation of thermally sensitive fission tracks from the spontaneous fission of ^{238}U in apatite crystals [*Naeser*, 1967]. For a recent review of the methodology, the reader is referred to *Gleadow et al.* [2002]. LA-ICP-MS based AFT analysis followed the procedure described in detail by *Gleadow et al.* [2015]. The footnote of Table 1 contains a summary of the analytical protocol used in this study.

Summary AFT data for the 17 samples analyzed are presented in Table 1 with individual grain and length data provided in Table S2. Central AFT ages, shown in Figure 1b, range from 311 ± 16 Ma to 470 ± 23 Ma and do not show a relationship with elevation (difference in elevation is <600 m). The confined MTLs vary from 11.1 ± 0.7 µm to 13.4 ± 0.3 µm with standard deviations ranging from 0.77 to 1.85 (Table 1). The short to moderate MTLs (the majority of samples have MTLs below 13 µm) and moderately broad, unimodal distributions (Table S2 includes a histogram of the confined track length distribution for each sample) suggest that these samples entered the AFT partial annealing zone (PAZ) prior to their apparent AFT ages, cooled linearly and experienced a moderate degree of annealing within the PAZ [*Brown et al.*, 1994]. The intra-sample age dispersion is low to moderate (≤21%) for all samples except one, 96Z-02 (27%), which is generally of poor quality (Table 1). This suggests that each sample is best approximated by a single population.

As the chemical composition of an apatite crystal is known to affect the thermal annealing rate of tracks [Green et al., 1986], the chemical compositions (Ca, P, F, Cl) of individual grains used for AFT dating were determined by electron microprobe or, where apatite yield was low, D_{par} (the long axis of a track etch pit parallel to the crystallographic c-axis) was used as a compositional proxy [Donelick, 1993; Burtner et al., 1994]. The Cl concentration is thought to exert the greatest influence such that high Cl apatites are more resistant to annealing and thus have higher closure temperatures [Green et al., 1986; Carlson et al., 1999; Barbarand et al., 2003]. In this dataset, there is no correlation between AFT age and D_{par} or Cl content, with D_{par} values ranging from 1.24-1.62 µm and Cl concentrations ranging from 0.01-0.02 wt%.

The spatial pattern of AFT ages suggests that the western region of the craton in Zimbabwe is the oldest land surface (Fig. 1b). AFT ages from this study are generally older than those reported for the cratonic interior from previous studies [Noble, 1997; Belton, 2006; Belton and Raab, 2010], and this trend becomes particularly apparent when comparison is made of existing AFT ages in close proximity to those of this study (Fig. 1b). This could be due to their location within the craton as the combined spatial AFT age pattern illustrates that ages systematically decrease towards the northern, eastern and southern margins of the craton (Fig. 1b). In some cases, however, it is most likely due to the sample being of poor quality with low apatite yield. For example, the very young AFT age from the center of the craton (red square in Figure 1b) was from a loosely consolidated Karoo sandstone that yielded only 9 grains and 11 track lengths [Belton and Raab, 2010].

3.2 (U-Th-Sm)/He analysis

(U-Th-Sm)/He thermochronology is based on the thermally sensitive accumulation of ^{4}He by the α decay of ^{238}U, ^{235}U, ^{232}Th and ^{147}Sm [*Farley*, 2002]. For detailed reviews of the AHe and ZHe methodology see *Farley and Stockli* [2002] and *Reiners* [2005], respectively. The full analytical procedures can be found in *Gleadow et al.* [2015], with analysis following the protocol for laser He extraction from single grains of *House et al.* [2000]. For each sample that yielded grains of suitable quality (>80 µm diameter, free of obvious inclusions and euhedral shape), one to five apatite and four to nine zircon grains were analyzed. Durango apatite and Fish Canyon Tuff zircon were used as internal standards to monitor analytical accuracy.

Due to the kinetic energy released during α decay of U and Th, an α-particle will travel on average ~19-22 µm and ~16-18 µm within an apatite or zircon crystal, respectively [*Ketcham et al.*, 2011]. Thus, the application of an α-ejection correction (F_T) to AHe and ZHe ages, proposed by *Farley et al.* [1996] to account for He lost from the grain by this process, has become common practice. However, recent work has demonstrated that where diffusional loss of He is dominant, as is the case in most slowly cooled cratonic regions that experience a protracted history through the He partial retention zone (PRZ), then the application of F_T will result in erroneously high (U-Th)/He ages [*Meesters and Dunai*, 2002; *Danišík et al.*, 2008]. Further, other competing effects, particularly U and Th zonation [*Hourigan et al.*, 2005; *Gautheron et al.*, 2012; *Orme et al.*, 2015], can complicate the He lost by α-ejection. Hence, uncorrected AHe and ZHe ages will be discussed (with corrected ages provided in Tables S3 and S5 for reference) and we shall account for the effects of α-ejection through the subsequent inverse thermal history modelling. Single grain AHe and ZHe ages are reported with a 6.2% (1σ) analytical uncertainty, which is based on the reproducibility of repeated Durango apatite measurements.

The characteristic prolonged residence within the PRZ also commonly results in significantly dispersed intra-sample single grain AHe and ZHe ages [*Fitzgerald et al.*, 2006]. This is because it provides the necessary time for the different He retentivity properties of individual grains to significantly diverge, due to many competing factors of dispersion, and create a span in (U-Th)/He ages. Hence, each grain can essentially act as an independent thermochronometer and provide insight into a different portion of the shared long-term thermal history. However, this means that a sample-averaged AHe/ZHe age is meaningless in these complex settings. Comprehensive summaries of the factors that cause dispersion in AHe datasets, with many directly applicable to the ZHe system [*Hourigan et al.*, 2005; *Danišík et al.*, 2017], can be found in *Fitzgerald et al.* [2006, Table 3] and *Wildman et al.*, [2016, Table 3]. In addition to those reported by these authors, recent studies have shown that chemical composition may also affect helium retentivity in the apatite system [*Gautheron et al.*, 2013; *Mbongo Djimbi et al.*, 2015].

In addition to excluding grains with obvious inclusions, we were able to account for, to some extent, the effects of radiation damage [*Shuster et al.*, 2006; *Guenthner et al.*, 2013], grain size [*Reiners and Farley*, 2001; *Reiners et al.*, 2004] and apatite fragmentation [*Brown et al.*, 2013] during our data interpretation and inverse thermal history modelling process.

Evaluation of the effect these sources of dispersion have had on our AHe and ZHe datasets is made separately in Sections 3.2.1 and 3.2.2, respectively. The effect of grain size is assessed by the proxy, equivalent spherical radius Rs (Rs = [3·R·L] / [2·{R+L}] where R = grain radius and L = grain length) [*Beucher et al.*, 2013]. Crystal radiation damage, caused by self-irradiation from its radiogenic elements, is assessed by the proxy, effective uranium concentration eU (eU = U + 0.235·Th) [*Flowers et al.*, 2007].

3.2.1 Apatite (U-Th-Sm)/He

AHe data for 57 single grains from 16 samples are provided in Table S3. Single grain AHe ages range from 99 ± 6 Ma to 474 ± 29 Ma and intra-sample dispersion is large (Fig. 3). In apatite, grain size and radiation damage are positively correlated with helium retentivity and thus closure temperature such that larger and more damaged grains will result in older AHe ages [*Reiners and Farley*, 2001; *Shuster et al.*, 2006]. In Figure 3, single grain AHe ages are shown as a function of the two proxies, eU and Rs.

There is no strong correlation between AHe age and eU except for a weak positive correlation in sample 96Z-38 and a steep positive correlation in 96Z-14 (Fig. 3). Similarly, the expected positive correlation between AHe age and Rs is generally absent except in samples 96Z-14 and 96Z-104 (Fig. 3). However, the lack of an apparent correlation could be due to the low number of data points available per sample (3-4 data points on average) or the high proportion of fragments in our dataset (Fig. 3). As thermal diffusion creates a non-uniform distribution of ^{4}He, fragmentation results in a miscalculation of the AHe age because the daughter to parent ratio in the broken grain will not equal that of the whole grain [*Brown et al.*, 2013]. Whether this effect results in an older or younger age than the original whole grain depends on the portion of the fragment (and He diffusion profile) remaining and whether the fragment has one termination (1T) or no terminations (0T) [*Brown et al.*, 2013]. Moreover, this effect causes the resultant apparent AHe age to deviate from the whole grain trajectory which can essentially decouple the effects of radiation damage and grain size and mask the expected relationship between AHe age with eU and Rs [*Brown et al.*, 2013]. The geological significance of the single grain AHe ages will be assessed in Section 4.2 where the AHe data are modelled alongside their corresponding AFT and ZHe data.

3.2.2 Zircon (U-Th)/He

ZHe data for 114 individual grains from 16 samples are provided in Table S5. Single grain ZHe ages range from 19 ± 1 Ma to 736 ± 46 Ma and intra-sample dispersion is large in the majority of samples. In zircon, grain size and radiation damage below an alpha-dose of ~2 x 10^{18} α/g behave similarly to that in apatite crystals [Guenthner et al., 2013]. However, above this damage threshold, interconnection of damage zones forms rapid diffusion pathways resulting in a corresponding decrease in the retentivity of helium within the mineral and thus the closure temperature [*Guenthner et al.*, 2013; *Ketcham et al.*, 2013]. Hence, crystal radiation damage could be positively or negatively correlated with single grain ZHe ages depending on the amount of accumulated radiation damage and the style of thermal history [Guenthner et al., 2013, 2014]. In our dataset, most samples exhibit some degree of negative correlation between ZHe age and eU, with eU values ranging from ~129-2910 ppm

(Fig. 4), but show no correlation with grain size (Fig. S6) or elevation (<600 m elevation change). The negative ZHe age-eU correlations suggest that these samples have experienced prolonged residence below temperatures of total damage annealing in order to allow appreciable variances in accumulated damage, proportional to their eU concentrations, and consequently ZHe age to develop [Guenthner et al., 2013]. In Figure 4, the dataset has been divided into regions that are assumed to share a common thermal history (i.e. same annealing history) in order to assist with interpretation. The broadly continuous negative age-eU correlations of each region, particularly in the central and southwestern regions, reinforces this assumption [Guenthner et al., 2014; Fig. 4] and indicates that radiation damage is the major control on ZHe age dispersion within this dataset [Guenthner et al., 2013].

In the southwestern (upper panel in Figure 4) and central (middle panel in Figure 4) regions of the craton, the correlation with age is strongly negative at eU values less than ~450 ppm, but flattens to form a broad long tail of ZHe ages between ~300-100 Ma. Within this age band, eU values are mostly between ~450-1000 ppm, although some zircons of this age range have lower (e.g. sample 96Z-01) and higher (e.g. sample 96Z-111) values (Fig. 4). Except for sample 96Z-26, samples from the northeastern region also show negative ZHe age-eU correlations (lower panel in Figure 4). However, the ZHe ages are generally younger and fall entirely within this broad ~300-100 Ma age range (even at eU values as low as ~180 ppm) with the exception of the very high eU sample 96Z-61 whose ages are as young as ~58-30 Ma (Fig. 4). This late Carboniferous to middle Cretaceous age population (upper grey boxes in Figure 4) accounts for 64% (n = 73) of the dated zircon grains. These zircons have eU values ranging from ~180-2700 ppm suggesting a span in individual effective closure temperatures. Thus, this could suggest that this age range represents a period of significant thermal rejuvenation. Coincidently, the upper limit of this age band corresponds to the initiation of Karoo sedimentation (~300 Ma) [*Catuneanu et al.*, 2005] and could represent thermal resetting of these zircons due to the shallow reburial of the craton. The fact that no ZHe ages in the northeastern region are older than Karoo times (lower panel of Figure 4) could imply that the Karoo cover was more extensive over this part of the craton and thus even the low eU (higher closure temperature) grains were reset. It is also worth noting here, although it will be discussed further in Section 5, that this significant ZHe age population is younger than the corresponding AFT central age range (~310-470 Ma) of these samples (Fig. 4).

Eleven high eU (~930-2910 ppm) zircons from samples 96Z-18 and 96Z-61 yield relatively consistent young Paleocene to Miocene (~58-19 Ma) ZHe ages (lower grey boxes in Figure 4) which are younger than the youngest AHe age (Fig. 4). The broadly uniform single grain ZHe ages of sample 96Z-61 (lower panel in Figure 4) are particularly significant. The eU concentrations span from ~1438-2911 ppm suggesting that these zircons possess a range of closure temperatures [*Guenthner et al.*, 2014; *Orme et al.*, 2016], however, the ZHe ages are fairly reproducible with an average of ~40 Ma (single grain ages range from 30 ± 2 Ma to 58 ± 4 Ma but most cluster between 30-42 Ma) (lower panel in Figure 4). Thus, the relative flatness of the ZHe age-eU trend of sample 96Z-61 (lower panel of Figure 4), despite the large variation in eU, implies that this sample experienced relatively rapid cooling through this range of closure temperatures [*Guenthner et al.*, 2014]. The high eU concentrations suggest the closure temperatures of these zircons are fairly low [*Guenthner et al.*, 2013, 2014]. The corresponding single grain AHe age of 345 ± 21 Ma and AFT central age of 311 ± 16 Ma as well as the low Cl content of the apatites (Table 1) indicate that the closure temperatures of the corresponding zircons are much less than 90-100 °C [*Burtner et al.*, 1994].

4 Inverse thermal history modelling

These LTT results reiterate that particularly in cratonic settings where zircons and apatites have experienced significant diffusional loss of helium and annealing of tracks due to prolonged residence at low temperatures, the measured apparent ages do not hold any particular geological meaning [*Wildman et al.*, 2017]. In this section, an inverse thermal history modelling approach is used to extract geological significance from this complex LTT dataset and generate the most plausible thermal history for the measured LTT ages and MTL data, as well as attempt to account for the effects of individual grain chemistry, accumulated radiation damage etc. on the resultant individual LTT age and thus thermal history.

4.1 Approach

In this study, the AHe, AFT and ZHe data were jointly inverted using the software, QTQt [*Gallagher*, 2012]. QTQt uses a Bayesian transdimensional Markov Chain Monte Carlo (MCMC) approach to invert the LTT data and produce a collection of accepted thermal histories where the complexity (although the Bayesian approach does favor simpler thermal models) and form of the thermal history are determined by the data [*Gallagher et al.*, 2009; *Gallagher*, 2012]. The Bayesian approach requires the user to define a time-temperature space in which the MCMC algorithm samples, and this along with any additional user-defined thermal history constraints (e.g. present day surface temperature and sample-specific geological constraints) as well as annealing and diffusion information are treated as prior probability information [*Gallagher*, 2012].

For each sample, the default time (oldest single grain age in the sample ± oldest single grain age in the sample) and temperature (100 ± 100 ºC) ranges were used for the general prior (model space). Although the time range of the model spaces spanned the last ~700-1500 Ma depending on the sample, an initial unconstrained model run for each sample found that the thermal histories were only well-constrained by the LTT data as far back as ~600-700 Ma. Hence, a broad initial constraint of 750 ± 100 Ma and 100 ± 100 ºC was then used to investigate what thermal history information each sample could provide from Pan-African (~750-500 Ma) times until the present day [after *Wildman et al.*, 2017]. The present-day surface temperature was set as 20 ± 10 ºC.

After each sample was modelled using this broad initial constraint, a subsequent model run was performed for those samples in close proximity to Karoo sediments. In the Mid-Zambezi basin, basal late Carboniferous to Early Permian glacial beds of the Dwyka Group unconformably overly Archean basement [*Orpen et al.*, 1989; *Johnson et al.*, 1996]. The Featherstone Karoo outlier in the center of the craton, adjacent to samples 96Z-01 and 96Z-02 (Figs. 1b and 2), is comprised of thin Triassic siltstones sitting unconformably on

Archean basement [*Stagman*, 1977; *Belton and Raab*, 2010]. Hence, in order to bring these basement rocks to near surface temperatures prior to the initiation of Karoo sedimentation in the different regions, an additional thermal history constraint of 300 ± 20 Ma and 20 ± 20 ºC was assigned to samples adjacent to the Karoo Mid-Zambezi Basin (96Z-105, 96Z-106 and 96Z-109 in Figure 5 and 96Z-14 in Figure 6) and a broader 285 ± 35 Ma and 20 ± 20 ºC constraint (in order to account for a potentially eroded earlier Karoo record) to those samples adjacent to the central Featherstone Karoo outlier (96Z-01 in Figure 6). Figure S7 presents the model outputs for these samples (96Z-01, 96Z-14, 96Z-105, 96Z-106 and 96Z-109) without the near-surface Karoo constraint to illustrate that the thermal histories presented in Figures 5 and 6 for these samples provide better constrained models that are consistent (within the 95% confidence intervals) with the thermal history outcomes of the initial model runs. For all samples, the thermal history models presented in Figures 5, 6 and 7 represent the relatively well-constrained portions for each sample, however, uncropped versions of the thermal history models are provided for reference in Figure S7.

For this study, the multi-compositional fission track annealing model of *Ketcham et al.* [2007b] was used to model the AFT data which attempts to account for the effects of chemical composition on annealing using a sample-average Cl/D_{par} kinetic value. All applicable single grain AFT data (Table S2) were used for QTQt inverse thermal history modelling, although the reported true fission track lengths were normalized for annealing and etching anisotropy using c-axis projection [*Donelick et al.*, 1999; *Ketcham et al.*, 2007a].

The AHe and ZHe data (Tables S3 and S5) were modelled using the radiation damage accumulation and annealing models for helium diffusion of *Gautheron et al.* [2009] and *Guenthner et al.* [2013], respectively. Where apatite fragments (all zircons were whole (2T) grains) were present, the 0T grains could not be modelled in QTQt using the currently implemented fragmentation model of *Brown et al.* [2013].

Intra-sample dispersion is large within our AHe and ZHe datasets and the He diffusion models and whole grain dating approach used in this study cannot account for many of the known factors of dispersion, such as zonation in zircon [*Guenthner et al.*, 2013] or chemical composition in apatite [*Gautheron et al.*, 2013]. Hence, less weight was given to the AHe and ZHe single grain ages by allowing them to be resampled from their already fairly conservative ±1σ age uncertainty (~6.2%). For this resampling method, a scaling factor is applied to the input uncertainty whereby those values with larger scaling factors (less precise), as is the case for our AHe and ZHe data, will have less influence on determining the thermal history but the observed ages will still be honored [*Gallagher et al.*, 2011]. Thus, this resampling method attempts to account for some of the undefined uncertainty which is not strictly known due to the limitations of the whole grain approach used to date the AHe and ZHe ages as well as the He diffusion models used to generate the inverse thermal histories. Moreover, as we have the greatest confidence in our AFT data, each sample was first modelled using solely the AFT data, then AFT with AHe data and finally adding the corresponding ZHe data so that a comparison could be made of all model outputs in order to ensure consistency. For the same reason, those samples that did not yield sufficient AFT data (96Z-02, 96Z-16, 96Z-18, 96Z-27 and 96Z-101; Fig. 1b and Table 1) were not modelled. All the thermal history models shown in Section 4.2 include AFT, AHe and ZHe data.

The MCMC sampler was run for 250,000 iterations with the first 50,000 discarded as burn-in [*Gallagher et al.*, 2009]. After each sample run, the acceptance rates of the proposed model parameters as well as the posterior sampling chain were checked to ensure satisfactory sampling [*Gallagher*, 2012]. The model output is represented by a collection of accepted thermal histories which are displayed as a color map indicating the posterior probability distribution of the thermal histories. We have chosen to display the expected model (weighted mean of the posterior distribution) as the most representative sample thermal history (see *Gallagher* [2012] and *Wildman et al.* [2015, 2016] for discussion) and the error on the expected model is illustrated by the 95% confidence intervals. The data fit of the models were assessed by plotting the observed ages against the predicted ages and comparing the data fit of the observed and predicted MTL distributions together with their associated uncertainties.

4.2 Modelling results and interpretation

A representative selection of inverse thermal history models from across the study area are presented in Figures 5, 6 and 7 with the additional thermal history models shown in Figure S7.

4.2.1 Post Pan-African cooling

In most of the reconstructed models, the thermal histories are poorly constrained prior to ~600 Ma (Fig. S7) suggesting the LTT data from the Zimbabwe Craton provide little thermal history information older than ~600 Ma. With the exception of a few samples from the central region of the craton, all samples record an Early Cambrian to Early Ordovician (~540-480 Ma) initiation of more rapid cooling with a clustering around an onset time of ~500 Ma (Fig. 5). The initiation of post-Pan-African cooling at ~500 Ma resulted in varying degrees of cooling (~90-140 ºC) and over durations varying between ~100-275 Myr (Figs. 5 and S7).

Some samples from the central region record an earlier transition to cooling in the Cryogenian (~680 Ma) (Fig. 6). Although the initiation of rapid cooling at ~540 Ma is not beyond the 95% confidence intervals of 96Z-104, an earlier initiation is moderately well constrained for 96Z-01 and 96Z-14 (Fig. 6). These samples experienced cooling on the order of approximately ~135-150 ºC from the Cryogenian until the early Carboniferous (~300 Ma) (Fig. 6) - i.e. the initiation of Karoo sedimentation. A significantly later initiation of rapid cooling in the Early Devonian (~415 Ma) is recorded by two samples from the northeast where cooling of ~110 ºC occurred over ~80 Ma (Fig. 7).

Figure 8 illustrates the spatial pattern of the initiation of cooling for modelled samples from this study. It is not clear whether the three samples that began cooling in the Cryogenian (blue in Figure 8) are representative of the entire central region or whether they are localized cooling signals. If representative of the central craton, the concentric pattern of the late Neoproterozoic (blue in Figure 8) to early Paleozoic (orange in Figure 8) cooling initiations could be suggestive that cooling resulted from denudation in response to radial upwelling of the surface from a deep mantle plume [*Lithgow-Bertelloni and Silver*, 1998]. However, although paleo-reconstructions and kimberlite magmatism are supportive of a mantle plume beneath this region of southern Africa in the Cambrian [*Jelsma et al.*, 2004; *Torsvik and Cocks*, 2013], there are no data supporting the presence of a late Neoproterozoic plume to initiate cooling in the central regions. Alternatively, and more likely, the late Neoproterozoic to early Paleozoic cooling initiation signals from across the study region represent the far-field response to the concurrent, progressive Pan-African collisional events that took place during the amalgamation of Gondwana between ~750-500 Ma [e.g. *Stern*, 1994; *Meert,* 2002; *Veevers*, 2003]. The inset map of Figure 8 shows the location of the Zimbabwe Craton and neighboring Pan-African orogenic belts within central Gondwana during the Cambrian. Intraplate stresses transmitted from surrounding continental collisions can travel significant distances and cause localized compression, uplift and denudation [e.g. *Holford et al.*, 2009]. Indeed, a similar stress propagation mechanism associated with Pangea assembly in the late Paleozoic was proposed by *Kasanzu et al.* [2016] to explain cooling signals recorded in the Tanzanian Craton. Further, *Moore et al.*[2008] and *Jelsma et al.*, [2009] would argue that stress transmission, as opposed to plume activity, was reasonable for Cambrian kimberlite magmatism.

The earlier Cryogenian (~680 Ma) age for the initiation of cooling for the three samples in the central region (Figs. 6 and 8) is coeval, and thus suggestive of a causative link, with the ~750-620 Ma East African Orogeny (EAO) events further north associated with the progressive closure of the Mozambique Ocean [Stern, 1994]. The more widespread ~500 Ma initiation of cooling (Figs. 5 and 8) was most likely caused by the more immediate effects of the adjacent ~600-500 Ma Kuunga orogenic events [Meert, 2002; inset of Fig. 8]. The coincident post-orogenic extension and magmatism (~533-486 Ma) observed in the Mozambique Belt to the east [Jacobs et al., 2008; Bingen et al., 2009; inset of Fig. 8], as discussed in Section 2, is supportive of this cooling signal recording post-orogenic denudation. Changes in the dominant stress regime from northwest-southeast oriented during the EAO [Veevers, 2003] to north-south oriented during the Kuunga Orogeny [Campbell et al., 1991] could be responsible for the different regions of stress transmission and earlier onset of cooling recorded by a few samples, which were perhaps located on lineaments preferentially susceptible to the EAO stress regime (dashed blue lines in Figure 8). These thermal history model results as well as the fact that no LTT ages from this study are older than ~750 Ma suggests that the majority of the Zimbabwe Craton, as opposed to just the eastern margin as proposed by Chaúque et al. [2017], was thermally reset during Pan-African times. Further, limited zircon U-Pb data from Archean basement samples in the study area indicate reclosure at even higher temperatures between ~900-800 Ma and ~600-480 Ma [*Wilson et al.*, 1995; *Söderlund et al.*, 2010], which were interpreted by *Wilson et al.*[1995] as reflecting Pan-African activity.

The widespread occurrence of the ~500 Ma onset of substantial cooling suggests that perhaps the entire region encompassing the current broad topographic high was rejuvenated during this time (the pale orange area in Figure 8 represents the inferred rejuvenated region based on the sampled data). If this rejuvenation was associated with intraplate compression, uplift and denudation then this suggests that this area of high elevation may have an ancient component related to Gondwana amalgamation. This is supported by the Cretaceous African reconstruction of Doucouré and de Wit [2003] where the Zimbabwe Craton is already a positive topographic feature, although at much lower elevations than it is now. More, these authors also postulated that some of the topographic features of Africa could have been caused by earlier Pan-African events, as suggested, at least in part, for the central region of the Zimbabwe Craton in this study.

The more rapid cooling event initiated in the Early Devonian that is recorded by two samples from the northeastern region appears to be fairly localized and overprints the regional cooling pattern (Fig. 8). A set of major strike-slip faults known as the Popoteke faults (Fig. 8), which parallel the NNE trend of the Great Dyke and are assumed to be part of the same fracture system (Fig. 2), run through this region of the craton [Wilson, 1990]. Both samples lie within this faulted region and thus could imply that structural reactivation, localized transpression and tectonic exhumation of the small uplifted block (red region in Figure 8) began at ~415 Ma. Indeed, *Wilson* [1990] discusses reactivation of the related Great Dyke fracture system during Pan-African times. The timing of reactivation is broadly coeval with the aforementioned thermal rejuvenation of the eastern margin of the Zimbabwe Craton [Vail, 1966; Manhica et al., 2001; Grantham et al., 2011; Chaúque et al., 2017] which could be related to a more temporally extensive post-Kuunga reactivation phase than currently recognized by limited zircon and monazite U-Pb data in the southern Mozambique Belt to the east [Jacobs et al., 2008; Bingen et al., 2009]. Thus, this potential reactivation signal could be related to this post-Kuunga activity.

As inferred from the thermal history models, the craton experienced variable but prolonged denudation throughout the Paleozoic (Figs. 5, 6 and 7). The few heat flow measurements available for the gneiss-granite-greenstone terrain of the Zimbabwe Craton suggest that the average geothermal gradient of the uppermost crust is ~14.1 °C/km [Nyblade et al., 1990]. If this present mean geothermal gradient provides a first-order approximation of the paleo-geothermal gradient of the region, the expected thermal history models (Figs. 5, 6 and 7) would imply that between ~5.5 km to ~10.6 km were exhumed from the craton during this period of post-Pan-African cooling. An alternative and perhaps more realistic possibility is that prior to this rejuvenation phase, the craton had a more extensive sedimentary cover of much lower thermal conductivity (i.e. elevated geothermal gradient) that would drastically reduce the amount of removed material required to produce the inferred cooling [Braun et al., 2016]. For instance, if we assume a geothermal gradient of 30 °C/km, this would reduce the required denuded material to ~2.5-5 km.

Predicting previous pathways for this denuded material is difficult, not only because it could have been transported and deposited in former neighboring regions of Gondwana but also because it could have been subsequently recycled and redistributed. Andersen et al. [2016] proposed that recycling is responsible for the lack of an Archean detrital zircon signature in Phanerozoic sedimentary cover sequences in southern Africa. However, within the Magondi Belt to the west of the craton (inset of Fig. 2), ~150-700 m of the Neoproterozoic to early Paleozoic sediments of the Sijarira Group are preserved [Stagman, 1977; Campbell et al., 1991; Hanson et al., 1994]. Hanson [2003] interpreted these sediments, as well as other similarly aged sediments across southern Africa, as syn-orogenic foreland basin deposits that resulted from Pan-African activity. Moreover, Ordovician to Devonian sediments of the Sinakumbe Group are preserved further west in southern Zambia [Nyambe and Utting, 1997]. This could imply that material eroding from the postulated topographic high of the Zimbabwe cratonic interior was transported and deposited to the west. However, as discussed by Key et al. [2015], the lack of extensive pre-Carboniferous Paleozoic sediments in southern Africa could also be due to this sedimentary cover being subsequently stripped and redistributed (potentially significant distances) by the late Carboniferous to Early Permian Dwyka glaciation which covered a large region of Gondwana [Visser, 1987].

With the exception of samples from the northeastern region of the craton (96Z -26, -29, -38, -61, -65, -101) and sample 96Z-109 from the far southwestern region, the current land surface of the craton has remained below 60 ºC (base of AFT PAZ) since at least the early Carboniferous (~350 Ma). This is similar to the findings of Wildman et al. [2017] from the cratonic interior of the Kaapvaal Craton where AHe and AFT data from two samples from the interior revealed a dominant post-Pan-African cooling phase followed by residence at low temperatures (<60 ºC) since the late Carboniferous.

4.2.2 Shallow Karoo burial and unroofing

The relatively younger ZHe ages and shortened AFT lengths provide insight into the more recent thermal histories across the craton, particularly so in the northeastern region where all ZHe ages are younger than their corresponding AHe and AFT ages. The inverse model results of samples from across the craton also support the aforementioned (Section 3.2.2) suggestion that the younger ZHe ages could be the result of thermal rejuvenation due to shallow reburial of the basement rocks by Karoo sediments (Figs. 5, 6 and 7). Although the exact temperature sensitivity of the ZHe system at these low temperatures is uncertain, the expected thermal history models frequently predict a period of gradual reheating following the initiation of Karoo sedimentation (~300 Ma) corresponding to reheating on the order of ~15-65 °C (Figs. 5, 6 and 7). Indeed, reheating of this magnitude is possible within the 95% confidence interval temperature ranges of samples 96Z-22 and 96Z-104, the few samples where the expected models do not indicate reheating. The present geothermal gradient of the crystalline basement does not provide a reasonable paleo-estimate for calculating the amount of denuded low conductivity Karoo cover. However, assuming an elevated paleo-geothermal gradient of 25-30 °C/km would suggest ~0.5-2.5 km of Karoo sediments were removed from the craton.

The removal of a thin Karoo cover is not unreasonable considering evidence suggests that a dominantly westwardly glacial and drainage system provided Karoo sediments to the basins of south-central Africa during at least the Permian to Triassic [*Oesterlen and Millsteed*, 1994; *Moore et al.*, 2009a; *Key et al.*, 2015] and preserved sediment thicknesses in the Mid-Zambezi basin to the west of the Zimbabwe Craton range from ~2 km to more than 4 km [*Campbell et al.*, 1991]. *Key et al.* [2015] proposed that a mountainous region over northern Mozambique and eastern Zimbabwe was the likely source region for the Karoo sediments. They suggested that these mountains remained from the aforementioned Himalayan-style Pan-African EAO [*Jacobs and Thomas*, 2004] and are today manifest as the Manica Highlands in eastern Zimbabwe [*Moore et al.*, 2017].

If this reheating signature does represent a previously more extensive Karoo cover over the Zimbabwe Craton then the transition from gradual heating to more rapid cooling at ~40-25 Ma in the majority of the expected thermal history models implies that denudation of this variably thick cover began in the late Paleogene (Figs. 5, 6 and 7). The fact that only extremely high eU zircon grains yield Paleogene-Neogene ZHe ages (samples 96Z-18 and 96Z-61 in Fig. 4) suggests that only grains that had accumulated substantial radiation damage were fully reset by this cooling phase. In previous AFT studies of Zimbabwe, a slight indication of a Paleogene cooling event was suggested by thermal history modelling, however, as cautioned by the authors, the event was at or below the temperature sensitivity limit of the AFT system [*Noble*, 1997; *Belton*, 2006; *Belton and Raab*, 2010]. Here we have shown that remarkably the ZHe system has the ability to more robustly constrain this Paleogene thermal event.

Independent support for this minor denudation phase comes from increased Oligocene terrigenous sedimentation in two of the depositional sinks of the Zimbabwe Craton, the Zambezi [*Walford et al.*, 2005] and Limpopo [*Burke and Gunnell*, 2008] deltas. High but variable fluxes of terrigenous sediment have continued until recent times in the Zambezi Delta [*Walford et al.*, 2005] and Southern Mozambique Basin (which includes the Limpopo Delta) [*Said et al.*, 2015] and are supportive of the gradual removal of Karoo sediments from the Zimbabwe Craton. Moreover, the onset of this denudation episode is also coeval and thus supportive of the ~43-33 Ma epeirogenic uplift event of the Ovamboland-Kalahari-Zimbabwe (OKZ) axis, which makes up the current central watershed (Figs. 1b and 8), proposed by *Moore et al.* [2009a, 2009b]. *Moore et al.* [2009a, 2009b] attributed this uplift to the propagation of stresses from a coincident major plate reorganization in the Indian Ocean spreading regime [*Reeves and De Wit*, 2000] as well as an increase in the spreading rate in the Atlantic Ocean [*Nürnberg and Müller*, 1991]. Alternatively, others have argued that Africa underwent major Cenozoic topographic development in response to a postulated ~40-30 Ma onset of mantle plume activity [e.g. *Partridge and Maud*, 1987; *Burke*, 1996; *Rudge et al.*, 2015]. Regardless of the magnitude or cause of this potential Cenozoic uplift phase, the lack of a Cenozoic signature in our AHe and AFT data suggest that the associated denudation of the Zimbabwe Craton was limited.

Interestingly, the cratonic interior of Zimbabwe does not appear to have been significantly thermally affected by events associated with the breakup of Gondwana in the Early Jurassic to Early Cretaceous [*Veevers*, 2012]. Gondwana breakup cooling signals dominate in the surrounding Limpopo Belt [*Belton and Raab*, 2010], Zambezi Belt [*Noble*, 1997] and eastern margin of the craton [*Belton*, 2006]. These authors mainly attributed these cooling signals to tectonic exhumation associated with reactivation of pre-existing structures [*Noble*, 1997; *Belton and Raab*, 2010]. Sample 96Z-65 is the only sample that shows a transition to cooling coincident with break up (~180 Ma) (Fig. S7) and this sample is located closest to the samples analyzed by Belton (2006) along the eastern margin of the craton (Fig. 1b). Thus, the thermal stability of the interior of the Zimbabwe Craton during Gondwana breakup illustrated by this study supports structural interpretations [*Daly et al.*, 1989; *Orpen et al.*, 1989; *Lenardic et al.*, 2000] that the cratonic regions of Africa were largely isolated from Gondwana breakup events.

5 'Inversion' of expected age relationships

In cratonic settings, the slight 'inversion' of AHe and AFT ages from the same sample is commonly observed [e.g. *Hendriks and Redfield*, 2005; *Green et al.*, 2006; *Danišík et al.*, 2008; *Kohn et al.*, 2009; *Flowers and Kelley*, 2011]. Indeed, it is almost expected considering the overlapping temperature sensitivities of the AHe (~30-90 ºC) [*Flowers et al.*, 2009] and AFT (~60-120 ºC) [*Wagner and Van den haute*, 1992] systems, the varying and potentially competing factors that influence He diffusion and track annealing, as well as the characteristic protracted cooling histories of cratonic settings which amplify age dispersion [e.g. *Fitzgerald et al.*, 2006].

Initial investigations of the ZHe system suggested that the closure temperature was ~180 °C [*Reiners et al.*, 2002, 2004; *Wolfe and Stockli*, 2010] and thus ZHe thermochronometry would produce ages older than AHe and AFT ages for the same sample. Subsequent experimental work by *Guenthner et al.* [2013] showed that due to the effects of radiation damage in zircon, the ZHe system can have temperature sensitivities that range from <0 ºC to ~220 ºC. However, ZHe ages that are younger than their corresponding AHe or AFT ages (i.e. the ZHe system is sensitive to lower temperatures) have been infrequently observed in previous work. *Brichau et al.* [2006] and *Bargnesi et al.* [2013] discussed ZHe ages that were younger than their corresponding AFT and AHe ages, respectively. However, the authors tentatively ascribed this inversion to zonation and did not investigate further. *Johnson et al.* [2017] showed that in one of their samples, ZHe ages were significantly younger than AHe ages and could be easily explained by the fact that the highly damaged nature of the zircons had resulted in closure temperatures of <50 °C. The reason such inverted ZHe ages have not been more frequently observed might in part be due to the lack of studies combining these three thermochronometers, particularly in cratonic settings where prolonged residence at the low temperatures required for substantial radiation damage to accumulate is typical. Hence, until the recent work of *Johnson et al.* [2017], the potential of highly damaged zircons to be an ultra-low-temperature thermochronometer has not been apparent.

In this study, with the exception of sample 96Z-16 for which there is no corresponding AFT or AHe data, all samples that have ZHe data show some degree of age inversion (Fig. 4). Of these samples, only 6 (out of 106) of the dated zircons yield ZHe single grain ages older than their corresponding AFT central ages (Fig. 4). Although some single grain AFT ages will be lower than their central age, this provides a reasonable comparison and is suggestive that a large majority of the zircons have lower temperature sensitivities than the corresponding AFT temperature ranges of the dated apatites. The presence of U and Th zonation can have a significant effect on ZHe ages [*Hourigan et al.*, 2005; *Guenthner et al.*, 2013] and is most likely contributing to scatter in the main ZHe age-eU trends (Fig. 4). Although due to the whole grain dating approach used in this study [*Gleadow et al.*, 2015] the potential effects of zonation cannot be further investigated, the strong negative ZHe age-eU correlations suggest that radiation damage is largely responsible for these 'inverted' ages (Fig. 4). This is even the case for some relatively low eU zircons such as the <500 ppm (as low as 179 ppm) grains of samples 96Z-01 and 96Z-65 (Fig. 4) suggesting that extreme accumulated damage is not required to cause 'inversion' in certain settings. Further, the ZHe temperature sensitivities of some samples, e.g. 96Z-01, are even lower than the corresponding AHe temperature sensitivity ranges (Figs. 3 and 4), however, a detailed comparison is more difficult due to the significant intra-sample scatter in both datasets (Figs. 3 and 4).

As there is no available zircon fission track (ZFT) data for these samples, we cannot assume rapid cooling from temperatures above the ZFT PAZ. Assuming this to be the threshold temperature for α-radiation damage annealing in zircon, and without Raman spectroscopy data, we are therefore unable to calculate an effective alpha dose for these samples following the procedures of *Guenthner et al.* [2013]. However, the lower closure temperatures for these zircons would suggest that they have approximate alpha doses well in excess of 4×10^{18} α/g, which is inferred to correspond to a closure temperature of ~90-100 °C according to *Guenthner et al.* [2013, Fig. 10]. The high eU grains of samples 96Z-18 and 96Z-61 and much younger ZHe ages would suggest they have much higher effective alpha doses and much lower closure temperatures.

The inverse thermal history model predictions revealed that the zircon radiation damage and accumulation model (ZRDAAM) implemented into QTQt is able to predict ZHe ages that are younger than their corresponding AFT central age. However, with the exception of the extreme eU grains of samples 96Z-61, -109 and -111 (Fig. 4), the ZHe age predictions are almost always slightly to substantially older than the observed ZHe ages (Figs. 5, 6 and 7). Moreover, in cases with extremely high eU zircon grains, the inverse modelling process was unable to honor both the AHe and ZHe ages. For instance in samples 96Z-61 (Fig. 7) and 96Z-109 (Fig. 5), the ZRDAAM was able to reproduce some of the young ZHe ages whilst honoring the corresponding AFT data but the corresponding AHe age prediction was near 0 Ma when the observed ages were >300 Ma (also see Fig. S7). In these thermal history scenarios, the inverse model required recent reheating to >80 °C which could explain why the AHe age was near 0 Ma.

An approach was proposed by *Guenthner et al.* [2013] to generate forward modelled ZHe age-eU correlations using their ZRDAAM and, by comparing the modelled and observed ZHe age-eU trends, deciphering the most likely thermal history. This approach has been used in numerous studies [*Guenthner et al.*, 2013, 2014; *Orme et al.*, 2016; *Powell et al.*, 2016; *Johnson et al.*, 2017] and was attempted in this study using the forward modelling capabilities of QTQt [*Gallagher*, 2012] and a specifically developed Python script for generating the predicted ZHe age-eU envelopes. The aim of utilizing this forward modelling approach for this study was to investigate if by adjusting individual portions of the entire (Archean-Recent) history whether it was possible to reproduce the young ZHe ages of the most extremely damaged zircons (in samples 96Z-18 and 96Z-61) whilst still honoring the corresponding AFT and AHe (i.e. not requiring recent reheating to >80 °C) data.

Figure 9 shows the forward thermal history model that honored the most observed data for each sample. The forward model of 96Z-61 predicts the onset of cooling in the Paleogene, similar to that predicted by a suite of inverse models from across the craton (Figs. 5, 6 and 7), although sample 96Z-18 predicts the onset of cooling to be in the latest Cretaceous. The predictions approach the observed ZHe age-eU trends and AFT data without requiring a recent reheating phase to >80 °C, however, it is still difficult to reproduce all of the observed data.

At high eU (>1000 ppm for 96Z-18 and >1500 ppm for 96Z-61), the ZRDAAM under-predicts the helium retentivity with near or below 0 Ma ages where the observed ages range from ~19-58 Ma (Fig. 9). The inverse modelling predictions for sample 96Z-61 also illustrate this for the youngest grains (Figs. 7 and S7). Thus, it appears that there are inconsistencies between the radiation damage accumulation and annealing models in either apatite [*Gautheron et al.*, 2009], zircon [*Guenthner et al.*, 2013] or both.

Similar discrepancies have been observed in previous studies where a flat trend of young ZHe ages with high eU has been difficult to reproduce [*Orme et al.*, 2016] and/or incompatible with corresponding AHe data [*Guenthner et al.*, 2014; *Johnson et al.*, 2017]. The reoccurring difficulty in reproducing high eU (in this case, >1000 ppm), young ZHe ages suggests that this incompatibility problem may be associated with the ZRDAAM for zircons that have accumulated substantial damage. Our results support the conclusions of *Johnson et al.* [2017] that the ZRDAAM under-predicts the retentivity of helium at high alpha doses and that further investigation of the ZRDAAM at the high radiation damage end is required. However, our inverse thermal history model results also reveal that for moderately damaged zircons, the ZRDAAM appears to consistently predict ZHe ages that are older than the observed data. This suggests that modifications may also be required for moderately damaged zircons. Unfortunately we are unable to assess how zonation could be affecting such modelling results, the effects of which could be significant as the ZRDAAM assumes a homogenous U and Th distribution [*Guenthner et al.*, 2013]. However, the consistent nature of the discrepancies between the observed and modelled data - the under-predictions at high eU observed in this study and that of *Johnson et al.* [2017] as well as the over-predictions at moderate eU revealed in this work – are supportive of a systematic model calibration issue.

The ZRDAAM is derived from a few well known datasets [*Reiners et al.*, 2002, 2004; *Nasdala et al.*, 2004; *Wolfe and Stockli*, 2010; *Guenthner et al.*, 2013], however, only two samples used in their model derivation have alpha doses that correspond to closure temperatures lower than the AFT system [*Guenthner et al.*, 2013], i.e. the approximate alpha doses of the zircons dated in this study. The ZRDAAM currently assumes that α-recoil damage anneals in the similar manner to fission tracks in zircon although, as cautioned by the authors themselves, this has not been tested [*Guenthner et al.*, 2013]. Indeed, if zircon behaves similarly to sphene, *Gleadow* [1978] found that α-recoil damage anneals at lower temperatures than fission tracks. Considering the ZFT system has a higher temperature sensitivity (~262-330 °C) [*Yamada et al.*, 2007], this could explain why the incompatibilities are most pronounced in highly damaged zircons whose temperature sensitivities are most dissimilar to those assumed by the model.

6 Conclusions

The multi-thermochronometer data and thermal history models reveal that the Zimbabwe Craton experienced two main cooling episodes during the Phanerozoic. Both cooling signals are interpreted to be the denudational response to surface uplift of the cratonic interior. The first and most significant period of cooling and denudation was triggered by stress transmission from the adjacent ~750-500 Ma Pan-African orogenic events associated with the amalgamation of Gondwana. This episode involved the thermal rejuvenation of all three LTT systems during a prolonged period of late Neoproterozoic/early Paleozoic to late Paleozoic denudation where, assuming a realistic but elevated paleo-geothermal gradient of 30 °C/km, ~2.5-5 km of material was stripped from the craton. Reheating of a large region of the craton began in the late Carboniferous when it was gradually reburied by a variable km-scale Karoo sedimentary cover. This thin Karoo blanket was subsequently removed during the second period of inferred denudation that began at ~40-25 Ma. This phase was triggered either by stress transmission from concurrent plate boundary processes or the onset of dynamic uplift associated with plume activity.

This study has reiterated the value of using a multi-thermochronometer approach whereby the three LTT systems used were able to reveal a history spanning the entire Phanerozoic. Within our dataset, the majority of ZHe ages are unexpectedly recurrently younger, even at relatively low eU, than their corresponding AHe and AFT ages. These results confirm previous suggestions that highly damaged zircons have the ability to reveal thermal history information at temperatures lower than that detectable by the AHe system [*Johnson et al.*, 2017]. However, this study reveals that it is not only extremely damaged zircons, such as our sample 96Z-61 and the comparable sample from *Johnson et al.* [2017], that have the ability to reveal younger thermal history information.

Although the thermal history inversions are able to reproduce most of the observed data, the ZRDAAM consistently predicts ZHe ages that are slightly to substantially older than the observed ages for moderately to highly damaged zircons. Moreover, the ZHe ages of extremely damaged zircons are incompatible with corresponding AHe ages using the current damage-diffusion models for apatite and zircon. This difficulty in reproducing young ZHe ages with high eU has been observed in other studies [e.g. *Guenthner et al.*, 2014; *Orme et al.*, 2016; *Johnson et al.*, 2017] and suggests that additional modification of the ZRDAAM is needed for high damage levels. However, the consistently older ZHe ages predicted by the ZRDAAM could suggest recalibration may also be required for moderate levels of damage.

Acknowledgements

Full sample details, data as well as all QTQt models and input data files can be found in the online supporting information. We gratefully acknowledge Abaz Alimanovic and Graham Hutchinson at the University of Melbourne for assistance with (U-Th)/He and electron microprobe analyses, respectively. The University of Melbourne thermochronology laboratory receives support under the National Collaborative Research Infrastructure Strategy AuScope program and the Education Investment Fund AGOS program. We thank Andy Moore, William Guenthner and Associate Editor Eva Enkelmann for their constructive and helpful reviews.

References

Allsopp, H. L., J. W. Bristow, and E. M. W. Skinner (1985), The Rb-Sr geochronology of the

Colossus kimberlite pipe, Zimbabwe, *Trans. Geol. Soc. South Africa*, *88*, 245–248.

Andersen, T., M. Kristoffersen, and M. A. Elburg (2016), How far can we trust provenance and crustal evolution information from detrital zircons? A South African case study, *Gondwana Res.*, *34*, 129–148, doi:10.1016/j.gr.2016.03.003.

Armstrong, R., and A. H. Wilson (2000), A SHRIMP U-Pb study of zircons from the layered sequence of the Great Dyke, Zimbabwe, and a granitoid anatectic dyke, *Earth Planet. Sci. Lett.*, *180*(1–2), 1–12, doi:10.1016/S0012-821X(00)00162-X.

Artemieva, I. M., and L. P. Vinnik (2016), Density structure of the cratonic mantle in Southern Africa: 1. Implications for dynamic topography, *Gondwana Res.*, *39*, 204–216, doi:10.1016/j.gr.2016.03.002.

Ault, A. K., R. M. Flowers, and S. A. Bowring (2009), Phanerozoic burial and unroofing history of the western Slave craton and Wopmay orogen from apatite (U–Th)/He thermochronometry, *Earth Planet. Sci. Lett.*, *284*(1–2), 1–11, doi:10.1016/j.epsl.2009.02.035.

Barbarand, J., A. Carter, I. Wood, and T. Hurford (2003), Compositional and structural control of fission-track annealing in apatite, *Chem. Geol.*, *198*(1–2), 107–137, doi:10.1016/S0009-2541(02)00424-2.

Barber, B. (1993), Notes on the isotopic dating off Karoo and younger lavas from the Zambezi valley and implications for sedimentation, *Ann. Zimbabwe Geol. Surv.*, *17*, 19–23.

Bargnesi, E. A., D. F. Stockli, N. Mancktelow, and K. Soukis (2013), Miocene core complex development and coeval supradetachment basin evolution of Paros, Greece, insights from (U–Th)/He thermochronometry, *Tectonophysics*, *595–596*(June), 165–182, doi:10.1016/j.tecto.2012.07.015.

Belton, D. X. (2006), The low temperature thermochronology of cratonic terranes, PhD Thesis, University of Melbourne, Melbourne, Australia.

Belton, D. X., and M. J. Raab (2010), Cretaceous reactivation and intensified erosion in the Archean–Proterozoic Limpopo Belt, demonstrated by apatite fission track thermochronology, *Tectonophysics*, *480*(1–4), 99–108, doi:10.1016/j.tecto.2009.09.018.

Beucher, R., R. W. Brown, S. Roper, F. Stuart, and C. Persano (2013), Natural age dispersion arising from the analysis of broken crystals. Part II. Practical application to apatite (U-Th)/He thermochronometry, *Geochim. Cosmochim. Acta*, *120*, 395–416, doi:10.1016/j.gca.2013.05.042.

Bingen, B., J. Jacobs, G. Viola, I. H. C. Henderson, Ø. Skår, R. Boyd, R. J. Thomas, A. Solli, R. M. Key, and E. X. F. Daudi (2009), Geochronology of the Precambrian crust in the Mozambique belt in NE Mozambique, and implications for Gondwana assembly, *Precambrian Res.*, *170*(3–4), 231–255, doi:10.1016/j.precamres.2009.01.005.

Braun, J., C. Stippich, and U. A. Glasmacher (2016), The effect of variability in rock thermal conductivity on exhumation rate estimates from thermochronological data, *Tectonophysics*, *690*, 288–297, doi:10.1016/j.tecto.2016.09.027.

Brichau, S., U. Ring, R. A. Ketcham, and A. Carter (2006), Constraining the long-term evolution of the slip rate for a major extensional fault system in the central Aegean, Greece, using thermochronology, *Earth Planet. Sci. Lett.*, *241*(1–2), 293–306.

Brown, R. W. (1992), A fission track thermochronology study of the tectonic and geomorphic development of the sub-aerial continental margins of southern Africa, PhD Thesis, La Trobe University, Melbourne, Australia.

Brown, R. W., D. J. Rust, M. A. Summerfield, A. J. W. Gleadow, and M. C. J. De Wit (1990), An early Cretaceous phase of accelerated erosion on the south-western margin of Africa: Evidence from apatite fission track analysis and the offshore sedimentary record, *Int. J. Radiat. Appl. Instrumentation. Part D. Nucl. Tracks Radiat. Meas.*, *17*(3), 339–350, doi:10.1016/1359-0189(90)90056-4.

Brown, R. W., M. A. Summerfield, and A. J. W. Gleadow (1994), Apatite fission track analysis: Its potential for the estimation of denudation rates and implications for models of long-term landscape development, in *Process models and theoretical geomorphology*, edited by M. J. Kirby, pp. 23–53, Wiley, Chichester.

Brown, R. W., A. J. W. Gleadow, and M. A. Summerfield (2002), Denudational history along a transect across the Drakensberg Escarpment of southern Africa derived from apatite fission track thermochronology, *J. Geophys. Res.*, *107*(B12), ETG 10-1-ETG 10-18, doi:10.1029/2001JB000745.

Brown, R. W., R. Beucher, S. Roper, C. Persano, F. Stuart, and P. Fitzgerald (2013), Natural age dispersion arising from the analysis of broken crystals. Part I: Theoretical basis and implications for the apatite (U–Th)/He thermochronometer, *Geochim. Cosmochim. Acta*, *122*, 478–497, doi:10.1016/j.gca.2013.05.041.

Brown, R. W., M. Summerfield, A. J. W. Gleadow, K. Gallagher, A. Carter, R. Beucher, and M. Wildman (2014), Intracontinental deformation in southern Africa during the Late Cretaceous, *J. African Earth Sci.*, *100*, 20–41, doi:10.1016/j.jafrearsci.2014.05.014.

Burke, K. (1996), The African plate, *South African J. Geol.*, *99*(4), 341–409.

Burke, K., and Y. Gunnell (2008), The African Erosion Surface: A Continental-Scale Synthesis of Geomorphology, Tectonics, and Environmental Change over the Past 180 Million Years, *Geol. Soc. Am. Mem.*, *201*, 1–66, doi:10.1130/2008.1201.

Burtner, R., A. Nigrini, and R. A. Donelick (1994), Thermochronology of Lower Cretaceous Source Rocks in the Idaho-Wyoming Thrust Belt, *Am. Assoc. Pet. Geol. Bull.*, *78*(10), 1613–1636.

Campbell, S. D. ., P. M. Oesterlen, T. G. Blenkinsop, P. E. J. Pitfield, and H. Munyanyiwa (1991), A provisional 1:2500000 Scale tectonic map and the tectonic evolution of Zimbabwe, *Ann. Zimbabwe Geol. Surv.*, *16*, 31–51.

Carlson, W. D., R. A. Donelick, and R. A. Ketcham (1999), Variability of apatite fission-track annealing kinetics I. Experimental results, *Am. Mineral.*, *84*(1999), 1213–1223, doi:0003-004X/99/0009–1213$05.00.

Catuneanu, O., H. Wopfner, P. G. Eriksson, B. Cairncross, B. S. Rubidge, R. M. H. Smith, and P. J. Hancox (2005), The Karoo basins of south-central Africa, *J. African Earth Sci.*, *43*(1–3), 211–253, doi:10.1016/j.jafrearsci.2005.07.007.

Chaúque, F. R., U. G. Cordani, D. L. Jamal, and A. T. Onoe (2017), The Zimbabwe Craton in Mozambique: A brief review of its geochronological pattern and its relation to the Mozambique Belt, *J. African Earth Sci.*, *129*, 366–379, doi:10.1016/j.jafrearsci.2017.01.021.

Cockburn, H. A. P., R. W. Brown, M. A. Summer, and M. A. Y. Seidl (2000), Quantifying passive margin denudation and landscape development using a combined fission-track thermochronology and cosmogenic isotope analysis approach, *Earth Planet. Sci. Lett.*, *179*, 429–435, doi:0012-821X/00/$.

Collins, A. S., and S. A. Pisarevsky (2005), Amalgamating eastern Gondwana: The evolution of the Circum-Indian Orogens, *Earth-Science Rev.*, *71*(3–4), 229–270, doi:10.1016/j.earscirev.2005.02.004.

Daly, M. C., J. Chorowicz, and J. D. Fairhead (1989), Rift basin evolution in Africa: the influence of reactivated steep basement shear zones, *Geol. Soc. London, Spec. Publ.*, *44*(1), 309–334, doi:10.1144/GSL.SP.1989.044.01.17.

Danišík, M., R. F. Sachsenhofer, V. A. Privalov, E. A. Panova, W. Frisch, and C. Spiegel (2008), Low-temperature thermal evolution of the Azov Massif (Ukrainian Shield–Ukraine) — Implications for interpreting (U–Th)/He and fission track ages from cratons, *Tectonophysics*, *456*(3–4), 171–179, doi:10.1016/j.tecto.2008.04.022.

Danišík, M., B. I. A. McInnes, C. L. Kirkland, B. J. McDonald, N. J. Evans, and T. Becker (2017), Seeing is believing: Visualization of He distribution in zircon and implications for thermal history reconstruction on single crystals, *Sci. Adv.*, *3*(2), e1601121, doi:10.1126/sciadv.1601121.

Donelick, R. A. (1993), Method of fission track analysis utilizing bulk chemical etching of apatite,

Donelick, R. A., R. A. Ketcham, and W. D. Carlson (1999), Variability of apatite fission-track annealing kinetics: II. Crystallographic orientation effects, *Am. Mineral.*, *84*, 1224–1234, doi:0003-004X/99/0009–1224$05.00.

Doucouré, C. M., and M. J. de Wit (2003), Old inherited origin for the present near-bimodal topography of Africa, *J. African Earth Sci.*, *36*(4), 371–388, doi:10.1016/S0899-5362(03)00019-8.

Duncan, R. A., P. R. Hooper, J. Rehacek, J. S. Marsh, and A. R. Duncan (1997), The timing and duration of the Karoo igneous event, southern Gondwana, *J. Geophys. Res.*, *102*(B8), 18127–18138, doi:10.1029/97JB00972.

Farley, K. A. (2002), (U-Th)/He Dating: Techniques, Calibrations, and Applications, *Rev. Mineral. Geochemistry*, *47*(1), 819–844, doi:10.2138/rmg.2002.47.18.

Farley, K. A., and D. F. Stockli (2002), (U-Th)/He Dating of Phosphates: Apatite, Monazite, and Xenotime, *Rev. Mineral. Geochemistry*, *48*(1), 559–577, doi:10.2138/rmg.2002.48.15.

Farley, K. A., R. A. Wolf, and L. T. Silver (1996), The effects of long alpha-stopping distances on (U-Th)/He ages, *Geochim. Cosmochim. Acta*, *60*(21), 4223–4229.

Fernandes, P., N. Cogné, D. M. Chew, B. Rodrigues, R. C. G. S. Jorge, J. Marques, D. Jamal, and L. Vasconcelos (2015), The thermal history of the Karoo Moatize-Minjova Basin, Tete Province, Mozambique: An integrated vitrinite reflectance and apatite fission track thermochronology study, *J. African Earth Sci.*, *112*, 55–72, doi:10.1016/j.jafrearsci.2015.09.009.

Fitzgerald, P. G., S. L. Baldwin, L. E. Webb, and P. B. O'Sullivan (2006), Interpretation of (U–Th)/He single grain ages from slowly cooled crustal terranes: A case study from the Transantarctic Mountains of southern Victoria Land, *Chem. Geol.*, *225*(1–2), 91–120, doi:10.1016/j.chemgeo.2005.09.001.

Flowers, R. M., and S. A. Kelley (2011), Interpreting data dispersion and "inverted" dates in apatite (U–Th)/He and fission-track datasets: An example from the US midcontinent, *Geochim. Cosmochim. Acta*, *75*(18), 5169–5186, doi:10.1016/j.gca.2011.06.016.

Flowers, R. M., and B. Schoene (2010), (U-Th)/He thermochronometry constraints on unroofing of the eastern Kaapvaal craton and significance for uplift of the southern African Plateau, *Geology*, *38*(9), 827–830, doi:10.1130/G30980.1.

Flowers, R. M., D. L. Shuster, B. P. Wernicke, and K. A. Farley (2007), Radiation damage control on apatite (U-Th)/He dates from the Grand Canyon region, Colorado Plateau, *Geology*, *35*(5), 447, doi:10.1130/G23471A.1.

Flowers, R. M., R. A. Ketcham, D. L. Shuster, and K. A. Farley (2009), Apatite (U-Th)/He thermochronometry using a radiation damage accumulation and annealing model, *Geochim. Cosmochim. Acta*, *73*(8), 2347–2365, doi:10.1016/j.gca.2009.01.015.

Flowers, R. M., K. A. Farley, and R. A. Ketcham (2015), A reporting protocol for thermochronologic modeling illustrated with data from the Grand Canyon, *Earth Planet. Sci. Lett.*, *432*, 425–435, doi:10.1016/j.epsl.2015.09.053.

Fritz, H. et al. (2013), Orogen styles in the East African Orogen: A review of the Neoproterozoic to Cambrian tectonic evolution, *J. African Earth Sci.*, *86*, 65–106.

Gallagher, K. (2012), Transdimensional inverse thermal history modeling for quantitative thermochronology, *J. Geophys. Res.*, *117*(B02408), 1–16, doi:10.1029/2011JB008825.

Gallagher, K., and R. W. Brown (1999), Denudation and uplift at passive margins: the record on the Atlantic Margin of southern Africa, *Philos. Trans. R. Soc. London A*, *357*, 835–859, doi:10.1098/rsta.1999.0354.

Gallagher, K., K. Charvin, S. Nielsen, M. Sambridge, and J. Stephenson (2009), Markov chain Monte Carlo (MCMC) sampling methods to determine optimal models, model resolution and model choice for Earth Science problems, *Mar. Pet. Geol.*, *26*(4), 525–

535, doi:10.1016/j.marpetgeo.2009.01.003.

Gallagher, K., T. Bodin, M. Sambridge, D. Weiss, M. Kylander, and D. Large (2011), Inference of abrupt changes in noisy geochemical records using transdimensional changepoint models, *Earth Planet. Sci. Lett.*, *311*(1–2), 182–194, doi:10.1016/j.epsl.2011.09.015.

Gautheron, C., L. Tassan-Got, J. Barbarand, and M. Pagel (2009), Effect of alpha-damage annealing on apatite (U–Th)/He thermochronology, *Chem. Geol.*, *266*(3–4), 157–170, doi:10.1016/j.chemgeo.2009.06.001.

Gautheron, C., L. Tassan-Got, R. A. Ketcham, and K. J. Dobson (2012), Accounting for long alpha-particle stopping distances in (U-Th-Sm)/He geochronology: 3D modeling of diffusion, zoning, implantation, and abrasion, *Geochim. Cosmochim. Acta*, *96*, 44–56, doi:10.1016/j.gca.2012.08.016.

Gautheron, C., J. Barbarand, R. A. Ketcham, L. Tassan-Got, P. van der Beek, M. Pagel, R. Pinna-Jamme, F. Couffignal, and M. Fialin (2013), Chemical influence on α-recoil damage annealing in apatite: Implications for (U–Th)/He dating, *Chem. Geol.*, *351*, 257–267, doi:10.1016/j.chemgeo.2013.05.027.

Gleadow, A. J. W. (1978), Anisotropic and variable track etching characteristics in natural sphenes, *Nucl. Track Detect.*, *2*, 105–117.

Gleadow, A. J. W., D. X. Belton, B. P. Kohn, and R. W. Brown (2002), Fission Track Dating of Phosphate Minerals and the Thermochronology of Apatite, *Rev. Mineral. Geochemistry*, *48*(1), 579–630, doi:10.2138/rmg.2002.48.16.

Gleadow, A. J. W., S. J. Gleadow, D. X. Belton, B. P. Kohn, M. S. Krochmal, and R. W. Brown (2009), Coincidence mapping - a key strategy for the automatic counting of fission tracks in natural minerals, in *Thermochronological Methods: From Palaeotemperature Constraints to Landscape Evolution Models*, vol. 324, edited by F. Lisker, B. Ventura, and U. A. Glasmacher, pp. 25–36, Geological Society, London, Special Publications.

Gleadow, A. J. W., M. Harrison, B. Kohn, R. Lugo-Zazueta, and D. Phillips (2015), Fish Canyon Tuff apatite: a new look at an old low-temperature thermochronology standard, *Earth Planet. Sci. Lett.*, *424*, 95–108.

Goscombe, B. D., and D. R. Gray (2008), Structure and strain variation at mid-crustal levels in a transpressional orogen: A review of Kaoko Belt structure and the character of West Gondwana amalgamation and dispersal, *Gondwana Res.*, *13*, 45–85, doi:10.1016/j.gr.2007.07.002.

Grantham, G. H., A. D. S. T. Manhica, R. A. Armstrong, F. J. Kruger, and M. Loubser (2011), New SHRIMP, Rb/Sr and Sm/Nd isotope and whole rock chemical data from central Mozambique and western Dronning Maud Land, Antarctica: Implications for the nature of the eastern margin of the Kalahari Craton and the amalgamation of Gondwana, *J. African Earth Sci.*, *59*(1), 74–100, doi:10.1016/j.jafrearsci.2010.08.005.

Green, P. F., I. R. Duddy, A. J. W. Gleadow, P. R. Tingate, and G. M. Laslett (1986), Thermal annealing of fission tracks in apatite 1. A qualitative description, *Chem. Geol. (Isotope Geosci. Sect.*, *59*, 237–253.

Green, P. F., P. V. Crowhurst, I. R. Duddy, P. Japsen, and S. P. Holford (2006), Conflicting (U-Th)/He and fission track ages in apatite: Enhanced He retention, not anomalous annealing behaviour, *Earth Planet. Sci. Lett.*, *250*(3–4), 407–427, doi:10.1016/j.epsl.2006.08.022.

Green, P. F., I. R. Duddy, P. Japsen, J. M. Bonow, and J. A. Malan (2015), Post-breakup burial and exhumation of the southern margin of Africa, *Basin Res.*, 1–32, doi:10.1111/bre.12167.

Guenthner, W. R., P. W. Reiners, R. A. Ketcham, L. Nasdala, and G. Giester (2013), Helium diffusion in natural zircon: radiation damage, anisotropy, and the interpretation of zircon (U-TH)/He thermochronology, *Am. J. Sci.*, *313*(March), 145–198, doi:10.2475/03.2013.01.

Guenthner, W. R., P. W. Reiners, and Y. Tian (2014), Interpreting date-eU correlations in zircon (U-Th)/He datasets: A case study from the Longmen Shan, China, *Earth Planet. Sci. Lett.*, *403*, 328–339, doi:10.1016/j.epsl.2014.06.050.

Haack, U. (1983), Reconstruction of the Cooling History of the Damara Orogen by Correlation of Radiometric Ages with Geography and Altitude, in *Intracontinental Fold Belts: Case Studies in the Variscan Belt of Europe and the Damara Belt in Namibia*, edited by H. Martin and F. W. Eder, pp. 873–884, Springer Berlin Heidelberg, Berlin, Heidelberg.

Haddon, I. G., and T. S. McCarthy (2005), The Mesozoic–Cenozoic interior sag basins of Central Africa: The Late-Cretaceous–Cenozoic Kalahari and Okavango basins, *J. African Earth Sci.*, *43*(1–3), 316–333, doi:10.1016/j.jafrearsci.2005.07.008.

Hanson, R. E. (2003), Proterozoic geochronology and tectonic evolution of southern Africa, in *Proterozoic East Gondwana: Supercontinent Assembly and Breakup*, edited by M. Yoshida, B. F. Windley, and S. Dasgupta, pp. 427–463, Geological Society, London, Special Publications.

Hanson, R. E., T. J. Wilson, and H. Munyanyiwa (1994), Geologic evolution of the neoproterozoic Zambezi orogenic belt in Zambia, *J. African Earth Sci.*, *18*(2), 135–150, doi:10.1016/0899-5362(94)90026-4.

Hanson, R. E., F. Worth, M. W. Martin, and S. A. Bowring (1998), U-Pb zircon age for the Umkondo dolerites, eastern Zimbabwe: 1.1 Ga large igneous province in southern Africa – East Antarctica and possible Rodinia correlations, *Geology*, *26*(12), 1143–1146.

Hargrove, U. S., R. E. Hanson, M. W. Martin, T. G. Blenkinsop, S. A. Bowring, N. Walker, and H. Munyanyiwa (2003), Tectonic evolution of the Zambezi orogenic belt: geochronological, structural, and petrological constraints from northern Zimbabwe, *Precambrian Res.*, *123*, 159–186, doi:10.1016/S0301-9268(03)00066-4.

Hasebe, N., J. Barbarand, K. Jarvis, A. Carter, and A. J. Hurford (2004), Apatite fission-track chronometry using laser ablation ICP-MS, *Chem. Geol.*, *207*(3–4), 135–145, doi:10.1016/j.chemgeo.2004.01.007.

Hendriks, B. W. H., and T. F. Redfield (2005), Apatite fission track and (U-Th)/He data from Fennoscandia: An example of underestimation of fission track annealing in apatite, *Earth Planet. Sci. Lett.*, *236*(1–2), 443–458, doi:10.1016/j.epsl.2005.05.027.

Holford, S. P., P. F. Green, I. R. Duddy, J. P. Turner, R. R. Hillis, and M. S. Stoker (2009), Regional intraplate exhumation episodes related to plate-boundary deformation, *Geol. Soc. Am. Bull.*, *121*(11–12), 1611–1628, doi:10.1130/B26481.1.

Hourigan, J. K., P. W. Reiners, and M. T. Brandon (2005), U-Th zonation-dependent alpha-ejection in (U-Th)/He chronometry, *Geochim. Cosmochim. Acta*, *69*(13), 3349–3365, doi:10.1016/j.gca.2005.01.024.

House, M. A., K. A. Farley, and D. Stockli (2000), Helium chronometry of apatite and titanite using Nd-YAG laser heating, *Earth Planet. Sci. Lett.*, *183*(3–4), 365–368, doi:10.1016/S0012-821X(00)00286-7.

Itano, K., T. Iizuka, Q. Chang, J.-I. Kimura, and S. Maruyama (2016), U–Pb chronology and geochemistry of detrital monazites from major African rivers: Constraints on the timing and nature of the Pan-African Orogeny, *Precambrian Res.*, *282*, 139–156, doi:10.1016/j.precamres.2016.07.008.

Jacobs, J., and R. J. Thomas (2004), Himalayan-type indenter-escape tectonics model for the southern part of the late Neoproterozoic–early Paleozoic East African– Antarctic orogen, *Geology*, *32*(8), 721–724, doi:10.1130/G20516.1.

Jacobs, J., B. Bingen, R. J. Thomas, W. Bauer, M. T. D. Wingate, and P. Feitio (2008), Early Palaeozoic orogenic collapse and voluminous late-tectonic magmatism in Dronning Maud Land and Mozambique: insights into the partially delaminated orogenic root of the East African–Antarctic Orogen?, *Geol. Soc. London, Spec. Publ.*, *308*(1), 69–90, doi:10.1144/SP308.3.

Jelsma, H., W. Barnett, S. Richards, and G. Lister (2009), Tectonic setting of kimberlites, *Lithos*, *112*, 155–165, doi:10.1016/j.lithos.2009.06.030.

Jelsma, H. A., M. J. de Wit, C. Thiart, P. H. G. . M. Dirks, G. Viola, I. J. Basson, and E. Anckar (2004), Preferential distribution along transcontinental corridors of kimberlites and related rocks of Southern Africa, *South African J. Geol.*, *107*(1–2), 301–324, doi:10.2113/107.1-2.301.

Johnson, J. E., R. M. Flowers, G. B. Baird, and K. H. Mahan (2017), “Inverted” zircon and apatite (U–Th)/He dates from the Front Range, Colorado: High-damage zircon as a low-temperature (<50 °C) thermochronometer, *Earth Planet. Sci. Lett.*, *466*, 80–90, doi:10.1016/j.epsl.2017.03.002.

Johnson, M. R., C. J. Van Vuuren, W. F. Hegenberger, R. Key, and U. Shoko (1996), Stratigraphy of the Karoo Supergroup in southern Africa: an overview, *J. African Earth*

Sci., *23*(1), 3–15.

Jones, D. L., R. A. Duncan, J. C. Briden, D. E. Randall, and C. Macniocaill (2001), Age of the Batoka basalts, northern Zimbabwe, and the duration of Karoo Large Igneous Province magmatism, *Geochemistry, Geophys. Geosystems*, *2*.

Kasanzu, C. H., B. Linol, M. J. Wit, R. Brown, C. Persano, and F. M. Stuart (2016), From source to sink in central Gondwana: Exhumation of the Precambrian basement rocks of Tanzania and sediment accumulation in the adjacent Congo basin, *Tectonics*, *35*, 2034–2051, doi:10.1002/2016TC004147.

Ketcham, R. A., A. Carter, R. A. Donelick, J. Barbarand, and A. J. Hurford (2007a), Improved measurement of fission-track annealing in apatite using c-axis projection, *Am. Mineral.*, *92*, 789–798, doi:10.2138/am.2007.2280.

Ketcham, R. A., A. Carter, R. A. Donelick, J. Barbarand, and A. J. Hurford (2007b), Improved modeling of fission-track annealing in apatite, *Am. Mineral.*, *92*(5–6), 799–810, doi:10.2138/am.2007.2281.

Ketcham, R. A., C. Gautheron, and L. Tassan-Got (2011), Accounting for long alpha-particle stopping distances in (U–Th–Sm)/He geochronology: Refinement of the baseline case, *Geochim. Cosmochim. Acta*, *75*(24), 7779–7791, doi:10.1016/j.gca.2011.10.011.

Ketcham, R. A., W. R. Guenthner, and P. W. Reiners (2013), Geometric analysis of radiation damage connectivity in zircon, and its implications for helium diffusion, *Am. Mineral.*, *98*(2–3), 350–360, doi:10.2138/am.2013.4249.

Key, R. M., F. P. D. Cotterill, and A. E. Moore (2015), The Zambezi River: An archive of tectonic events linked to the amalgamation and disruption of Gondwana and subsequent evolution of the African plate, *South African J. Geol.*, *118*, 425–438, doi:10.2113/gssajg.118.4.425.

Kohn, B. P., M. Lorencak, A. J. W. Gleadow, F. Kohlmann, A. Raza, K. G. Osadetz, and P. Sorjonen-Ward (2009), A reappraisal of low-temperature thermochronology of the eastern Fennoscandia Shield and radiation-enhanced apatite fission-track annealing, *Geol. Soc. London, Spec. Publ.*, *324*(1), 193–216, doi:10.1144/SP324.15.

Kounov, A., G. Viola, M. J. de Wit, and M. Andreoli (2008), A Mid Cretaceous paleo-Karoo River valley across the Knersvlakte plain (northwestern coast of South Africa): Evidence from apatite fission-track analysis, *South African J. Geol.*, *111*(4), 409–420, doi:10.2113/gssajg.111.4.409.

Kounov, A., G. Viola, M. de Wit, and M. A. G. Andreoli (2009), Denudation along the Atlantic passive margin: new insights from apatite fission-track analysis on the western coast of South Africa, *Geol. Soc. London, Spec. Publ.*, *324*(1), 287–306, doi:10.1144/SP324.19.

Kounov, A., G. Viola, I. Dunkl, and H. E. Frimmel (2013), Southern African perspectives on the long-term morpho-tectonic evolution of cratonic interiors, *Tectonophysics*, *601*, 177–191, doi:10.1016/j.tecto.2013.05.009.

Kröner, A. (1977), Precambrian mobile belts of southern and eastern Africa - ancient sutures or sites of ensialic mobility? A case for crustal evolution towards plate tectonics, *Tectonophysics*, *40*, 101–135.

Lenardic, A., L. Moresi, and H. Mühlhaus (2000), The role of mobile belts for the longevity of deep cratonic lithosphere: The crumple zone model, *Geophys. Res. Lett.*, *27*(8), 1235–1238, doi:10.1029/1999GL008410.

Lister, L. A. (1987), The Erosion Surfaces of Zimbabwe, *Zimbabwe Geol. Surv.*, (90), 163.

Lithgow-Bertelloni, C., and P. G. Silver (1998), Dynamic topography, plate driving forces and the African superswell, *Nature*, *395*(September), 269–272.

Lorencak, M., B. P. Kohn, K. G. Osadetz, and A. J. W. Gleadow (2004), Combined apatite fission track and (U–Th)/He thermochronometry in a slowly cooled terrane: results from a 3440-m-deep drill hole in the southern Canadian Shield, *Earth Planet. Sci. Lett.*, *227*(1–2), 87–104, doi:10.1016/j.epsl.2004.08.015.

Luft, F. F., J. L. Luft Jr, F. Chemale Jr, M. L. M. V Lelarge, and J. N. Ávila (2005), Post-Gondwana break-up record constraints from apatite fission track thermochronology in NW Namibia, *Radiat. Meas.*, *39*, 675–679, doi:10.1016/j.radmeas.2004.08.010.

Manhica, A. D. S. T., G. H. Grantham, R. A. Armstrong, P. G. Guise, and F. J. Kruger (2001), Polyphase deformation and metamorphism at the Kalahari Craton- Mozambique Belt boundary, in *Continental Reactivation and Reworking*, edited by J. A. Miller, R. E. Holdsworth, I. S. Buick, and M. Hand, pp. 303–322, Geological Society, London, Special Publications.

Mbongo Djimbi, D., C. Gautheron, J. Roques, L. Tassan-Got, C. Gerin, and E. Simoni (2015), Impact of apatite chemical composition on (U-Th)/He thermochronometry: An atomistic point of view, *Geochim. Cosmochim. Acta*, *167*, 162–176, doi:10.1016/j.gca.2015.06.017.

Meert, J. G. (2002), *A synopsis of events related to the assembly of the eastern Gondwana*.

Meesters, A. G. C. A., and T. J. Dunai (2002), Solving the production–diffusion equation for finite diffusion domains of various shapes Part I. Implications for low-temperature (U–Th)/He thermochronology, *Chem. Geol.*, *186*, 333–344.

Molnar, P., P. C. England, and C. H. Jones (2015), Mantle dynamics, isostasy, and the support of high terrain, *J. Geophys. Res. Solid Earth*, *120*, 1932–1957, doi:10.1002/2014JB011724.Received.

Moore, A. E. (1999), A reappraisal of epeirogenic flexure axes in southern Africa, *South African J. Geol.*, *102*(4), 363–376.

Moore, A. E., T. Blenkinsop, and F. P. D. Cotterill (2008), Controls on post-Gondwana alkaline volcanism in Southern Africa, *Earth Planet. Sci. Lett.*, *268*, 151–164, doi:10.1016/j.epsl.2008.01.007.

Moore, A. E., F. P. D. Cotterill, T. Broderick, and D. Plowes (2009a), Landscape evolution in

Zimbabwe from the Permian to present, with implications for kimberlite prospecting, *South African J. Geol.*, *112*(1), 65–88, doi:10.2113/gssajg.112.1.65.

Moore, A. E., T. Blenkinsop, and F. P. D. Cotterill (2009b), Southern African topography and erosion history: plumes or plate tectonics?, *Terra Nov.*, *21*(4), 310–315, doi:10.1111/j.1365-3121.2009.00887.x.

Moore, A. E., T. Blenkinsop, and F. P. D. Cotterill (2012), Dynamic evolution of the Zambezi-Limpopo watershed, Central Zimbabwe, *South African J. Geol.*, *115*(4), 551–560, doi:10.2113/gssajg.115.4.

Moore, A. E., F. P. D. Cotterill, and R. M. Key (2017), A geomorpholic and geological framework for the interpretation of species diversity and endemism in the Manica Highlands, *Kirkia*, *19*(January), 1–16.

Naeser, C. W. (1967), The use of apatite and sphene for fission track age determinations, *Geol. Soc. Am. Bull.*, *78*(December), 1523–1526.

Nasdala, L., P. W. Reiners, J. I. Garver, A. K. Kennedy, R. A. Stern, E. Balan, and R. Wirth (2004), Incomplete retention of radiation damage in zircon from Sri Lanka, *Am. Mineral.*, *89*(1), 219–231, doi:10.2138/am-2004-0126.

Nicolaysen, L. O., A. J. Burger, and R. L. Johnson (1962), The age of the Shawa carbonatite complex, *Trans. Geol. Soc. South Africa*, *65*, 293–294.

Noble, W. P. (1997), Post Pan African tectonic evolution of eastern Africa: An apatite fission track study, PhD Thesis, La Trobe University, Melbourne, Australia.

Nürnberg, D., and R. D. Müller (1991), The tectonic evolution of the South Atlantic from Late Jurassic to present, *Tectonophysics*, *191*(1–2), 27–53, doi:10.1016/0040-1951(91)90231-G.

Nyambe, I. A., and J. Utting (1997), Stratigraphy and palynostratigraphy, Karoo Supergroup (Permian and Triassic), mid-Zambezi Valley, southern Zambia, *J. African Earth Sci.*, *24*(4), 563–583, doi:10.1016/S0899-5362(97)00081-X.

Nyblade, A. A., H. N. Pollack, D. L. Jones, F. Podmore, and M. Mushayandebvu (1990), Terrestrial heat flow in east and southern Africa, *J. Geophys. Res.*, *95*(B11), 17371–17384, doi:10.1029/JB095iB11p17371.

Oberthur, T., D. W. Davis, T. G. Blenkinsop, and A. Hohndorf (2002), Precise U–Pb mineral ages , Rb–Sr and Sm–Nd systematics for the Great Dyke, Zimbabwe — constraints on late Archean events in the Zimbabwe craton and Limpopo belt, *Precambrian Res.*, *113*, 293–305.

Oesterlen, P. M., and B. D. Millsteed (1994), Lithostratigraphy, palaeontology, and sedimentary environments of the western Cabora Bassa Basin, Lower Zambezi Valley, Zimbabwe, *South African J. Geol.*, *97*(2), 205–224.

Orme, D. A., W. Reiners, Peter, J. K. Hourigan, and B. Carrapa (2015), Effects of inherited cores and magmatic overgrowths in zircon (U-Th)/He ages and age-eU trends from

Greater Himalyan sequence rocks, Mount Everest region, Tibet, *Geochemistry, Geophys. Geosystems*, *16*, 2499–2507, doi:10.1002/2014GC005684.Key.

Orme, D. A., W. R. Guenthner, A. K. Laskowski, and P. W. Reiners (2016), Long-term tectonothermal history of Laramide basement from zircon–He age-eU correlations, *Earth Planet. Sci. Lett.*, *453*, 119–130, doi:10.1016/j.epsl.2016.07.046.

Orpen, J. L., C. J. Swain, C. Nugent, and P. . Zhou (1989), Wrench-fault and half-graben tectonics in the development of the Palaeozoic Zambezi Karoo Basins in Zimbabwe — the "Lower Zambezi" and "Mid-Zambezi" basins respectively — and regional implications, *J. African Earth Sci.*, *8*(2/3/4), 215–229, doi:10.1016/S0899-5362(89)80026-0.

Partridge, T. C., and R. R. Maud (1987), Geomorphic evolution of Africa since the Mesozoic, *South African J. Geol.*, *90*, 197–208.

Paton, C., J. Hellstrom, B. Paul, J. Woodhead, and J. Hergt (2011), Iolite: Freeware for the visualisation and processing of mass spectrometric data, *J. Anal. At. Spectrom.*, *26*(12), 2508–2518, doi:10.1039/C1JA10172B.

Powell, J., D. Schneider, D. Stockli, and K. Fallas (2016), Zircon (U-Th)/He thermochronology of Neoproterozoic strata from the Mackenzie Mountains, Canada: Implications for the Phanerozoic exhumation and deformation history of the northern Canadian Cordillera, *Tectonics*, *35*, 1–27, doi:10.1002/2015TC003989.Received.

Raab, M. J., R. W. Brown, K. Gallagher, A. Carter, and K. Weber (2002), Late Cretaceous reactivation of major crustal shear zones in northern Namibia: constraints from apatite fission track analysis, *Tectonophysics*, *349*(1–4), 75–92, doi:10.1016/S0040-1951(02)00047-1.

Raab, M. J., R. W. Brown, K. Gallagher, K. Weber, and A. J. W. Gleadow (2005), Denudational and thermal history of the Early Cretaceous Brandberg and Okenyenya igneous complexes on Namibia's Atlantic passive margin, *Tectonics*, *24*(3), 1–15, doi:10.1029/2004TC001688.

Reeves, C., and M. De Wit (2000), Making ends meet in Gondwana: Retracing the transforms of the Indian Ocean and reconnecting continental shear zones, *Terra Nov.*, *12*(6), 272–280, doi:10.1046/j.1365-3121.2000.00309.x.

Reiners, P. W. (2005), Zircon (U-Th)/He Thermochronometry, edited by P. W. Reiners and T. A. Ehlers, *Rev. Mineral. Geochemistry*, *58*, 151–179, doi:10.2138/rmg.2005.58.6.

Reiners, P. W., and K. A. Farley (2001), Influence of crystal size on apatite (U-Th)/He thermochronology: an example from the Bighorn Mountains, Wyoming, *Earth Planet. Sci. Lett.*, *188*, 413–420.

Reiners, P. W., K. A. Farley, and H. J. Hickes (2002), He diffusion and (U-Th)/He thermochronometry of zircon: Initial results from Fish Canyon Tuff and Gold Butte, *Tectonophysics*, *349*(1–4), 297–308, doi:10.1016/S0040-1951(02)00058-6.

Reiners, P. W., T. L. Spell, S. Nicolescu, and K. A. Zanetti (2004), Zircon (U-Th)/He thermochronometry: He diffusion and comparisons with 40Ar/39Ar dating, *Geochim. Cosmochim. Acta*, *68*(8), 1857–1887, doi:10.1016/j.gca.2003.10.021.

Reiners, P. W., T. A. Ehlers, and P. K. Zeitler (2005), Past, Present, and Future of Thermochronology, in *Low-Temperature Thermochronology: Techniques, Interpretations and Applications,* vol. 58, edited by W. Reiners, Peter and Ehlers, pp. 1–18.

Rudge, J. F., G. G. Roberts, N. J. White, and C. N. Richardson (2015), Uplift histories of Africa and Australia from linear inverse modeling of drainage inventories, *J. Geophys. Res. Earth Surf.*, *120*(5), 894–914, doi:10.1002/2014JF003297.

Said, A., C. Moder, S. Clark, and B. Ghorbal (2015), Cretaceous-Cenozoic sedimentary budgets of the Southern Mozambique Basin: implications for uplift history of the South African Plateau, *J. African Earth Sci.*, doi:10.1016/j.jafrearsci.2015.05.007.

Shuster, D. L., R. M. Flowers, and K. A. Farley (2006), The influence of natural radiation damage on helium diffusion kinetics in apatite, *Earth Planet. Sci. Lett.*, *249*(3–4), 148–161, doi:10.1016/j.epsl.2006.07.028.

Smith, C. B., K. Sims, L. Chimuka, A. Duffin, A. D. Beard, and R. Townend (2004), Kimberlite metasomatism at Murowa and Sese pipes, Zimbabwe, *Lithos*, *76*(1–4), 219–232, doi:10.1016/j.lithos.2004.03.009.

Söderlund, U., A. Hofmann, M. B. Klausen, J. R. Olsson, R. E. Ernst, and P.-O. Persson (2010), Towards a complete magmatic barcode for the Zimbabwe craton: Baddeleyite U-Pb dating of regional dolerite dyke swarms and sill complexes, *Precambrian Res.*, *183*, 388–398, doi:10.1016/j.precamres.2009.11.001.

Stagman, J. G. (1977), Provisional Geological Map of Zimbabwe (reprinted 1994),

Stanley, J. R., R. M. Flowers, and D. R. Bell (2013), Kimberlite (U-Th)/He dating links surface erosion with lithospheric heating, thinning, and metasomatism in the southern African Plateau, *Geology*, *41*(12), 1243–1246, doi:10.1130/G34797.1.

Stanley, J. R., R. M. Flowers, and D. R. Bell (2015), Erosion patterns and mantle sources of topographic change across the southern African Plateau derived from the shallow and deep records of kimberlites, *Geochemistry, Geophys. Geosystems*, *16*, 3235–3256, doi:10.1002/2015GC005969.Received.

Stern, R. J. (1994), Arc Assembly and Continental Collision in the Neoproterozoic East African Orogen: Implications for the Consolidation of Gondwanaland, *Annu. Rev. Earth Planet. Sci.*, *22*, 319–351.

Thomas, D. S. G., and P. A. Shaw (1988), Late Cainozoic drainage evolution in the Zambezi basin: Geomorphological evidence from the Kalahari rim, *J. African Earth Sci.*, *7*(4), 611–618, doi:10.1016/0899-5362(88)90111-X.

Thomas, D. S. G., and P. A. Shaw (1990), The deposition and development of the Kalahari Group sediments, Central Southern Africa, *J. African Earth Sci.*, *10*(1/2), 187–197, doi:10.1016/0899-5362(90)90054-I.

Tinker, J., M. de Wit, and R. Brown (2008), Mesozoic exhumation of the southern Cape, South Africa, quantified using apatite fission track thermochronology, *Tectonophysics*, *455*(1–4), 77–93, doi:10.1016/j.tecto.2007.10.009.

Du Toit, A. L. (1933), Crustal movements as a factor in the geographical evolution of South Africa, *South African Geogr. J.*, *16*, 1–33.

Torsvik, T. H., and L. R. M. Cocks (2013), Gondwana from top to base in space and time, *Gondwana Res.*, *24*(3–4), 999–1030, doi:10.1016/j.gr.2013.06.012.

Vail, J. R. (1966), Zones of Progressive Regional Metamorphism Across the Western Margin of the Mozambique Belt in Rhodesia and Mozambique, *Geol. Mag.*, *103*(3), 231–239, doi:https://doi.org/10.1017/S0016756800052808.

Veevers, J. J. (2003), Pan-African is Pan-Gondwanaland: Oblique convergence drives rotation during 650–500 Ma assembly, *Geology*, *31*, 501–504, doi:10.1130/0091-7613(2003)031<0501.

Veevers, J. J. (2012), Reconstructions before rifting and drifting reveal the geological connections between Antarctica and its conjugates in Gondwanaland, *Earth-Science Rev.*, *111*(3–4), 249–318, doi:10.1016/j.earscirev.2011.11.009.

Vermeesch, P. (2009), RadialPlotter: a Java application for fission track, luminescence and other radial plots, *Radiat. Meas.*, *44*(4), 409–410.

Vinyu, M. L., R. E. Hanson, M. W. Martin, S. A. Bowring, H. A. Jelsma, M. A. Krol, and P. H. G. M. Dirks (1999), U-Pb and 40Ar/39Ar geochronological constraints on the tectonic evolution of the easternmost part of the Zambezi orogenic belt, northeast Zimbabwe, *Precambrian Res.*, *98*(1–2), 67–82, doi:10.1016/S0301-9268(99)00039-X.

Visser, J. N. J. (1987), The paleogeography of part of southwestern Gondwana during the Permo-Carboniferous glaciation, *Palaeogeogr. Palaeoclimatol. Palaeoecol.*, *61*, 205–219.

Wagner, G. A., and P. Van den haute (1992), *Fission-Track Dating*, Enke Verlag/Kluwer Academic Publishers, Dordrecht.

Walford, H. L., N. J. White, and J. C. Sydow (2005), Solid sediment load history of the Zambezi Delta, *Earth Planet. Sci. Lett.*, *238*(1–2), 49–63, doi:10.1016/j.epsl.2005.07.014.

Wildman, M., R. Brown, R. Watkins, A. Carter, A. J. W. Gleadow, and M. Summerfield (2015), Post break-up tectonic inversion across the southwestern cape of South Africa: New insights from apatite and zircon fission track thermochronometry, *Tectonophysics*, *654*, 30–55, doi:10.1016/j.tecto.2015.04.012.

Wildman, M., R. Brown, R. Beucher, C. Persano, F. Stuart, K. Gallagher, J. Schwanethal, and A. Carter (2016), The chronology and tectonic style of landscape evolution along the elevated Atlantic continental margin of South Africa resolved by joint apatite fission track and (U-Th-Sm)/He thermochronology, *Tectonics*, *35*(3), 511–545, doi:10.1002/2015TC004042.

Wildman, M., R. Brown, C. Persano, R. Beucher, F. M. Stuart, V. Mackintosh, K. Gallagher, J. Schwanethal, and A. Carter (2017), Contrasting Mesozoic evolution across the boundary between on and off craton regions of the South African plateau inferred from apatite fission track and (U-Th-Sm)/He thermochronology, *J. Geophys. Res. Solid Earth*, *122*, 1–31, doi:10.1002/2016JB013478.

Wilson, J. F. (1990), A craton and its cracks: some of the behaviour of the Zimbabwe block from the Late Archaean to the Mesozoic in response to horizontal movements, and the significance of some of its mafic dyke fracture patterns, *J. African Earth Sci. (and Middle East)*, *10*(3), 483–501, doi:10.1016/0899-5362(90)90101-J.

Wilson, J. F., R. W. Nesbitt, and C. M. Fanning (1995), Zircon geochronology of Archaean felsic sequences in the Zimbabwe craton: a revision of greenstone stratigraphy and a model for crustal growth, edited by M. P. Coward and A. C. Ries, *Geol. Soc. London, Spec. Publ.*, *95*(1), 109–126.

Wolfe, M. R., and D. F. Stockli (2010), Zircon (U-Th)/He thermochronometry in the KTB drill hole, Germany, and its implications for bulk He diffusion kinetics in zircon, *Earth Planet. Sci. Lett.*, *295*(1–2), 69–82, doi:10.1016/j.epsl.2010.03.025.

Yamada, R., M. Murakami, and T. Tagami (2007), Statistical modelling of annealing kinetics of fission tracks in zircon; Reassessment of laboratory experiments, *Chem. Geol.*, *236*(1–2), 75–91, doi:10.1016/j.chemgeo.2006.09.002.

Sample Number	No. of grains	N_s[a]	ρ_s[b] (10^5 cm^{-2})	^{238}U[c] (ppm)	Dispersion (%)	Pooled age (Ma ± 1σ)	Central age (Ma ± 1σ)	N_L[d]	MTL[e] (µm ± SE)	SD[f] (µm)	D_{par}[g] (µm)	Cl[h] (wt %)
96Z-01	25	1418	19.751	9.27	19	433 ± 26	443 ± 22	82	12.7 ± 0.2	1.33	1.37	0.02
96Z-02	6	635	100.503	58.08	27	451 ± 52	415 ± 57	8	11.1 ± 0.7	1.85	1.41	-
96Z-14	27	1910	7.148	3.40	17	449 ± 19	466 ± 20	86	12.6 ± 0.2	1.37	1.38	0.01
96Z-18	4	561	43.217	20.85	7	418 ± 27	418 ± 27	21	13.4 ± 0.3	1.51	1.62	-
96Z-22	20	3446	36.474	19.28	15	422 ± 18	433 ± 18	82	13.1 ± 0.1	1.03	1.53	0.02
96Z-26	26	4297	64.730	35.28	4	393 ± 9	391 ± 8	90	12.6 ± 0.1	0.97	1.48	0.01
96Z-29	22	1111	23.743	16.42	9	318 ± 12	319 ± 13	51	11.4 ± 0.2	1.38	1.43	0.01
96Z-38	22	5143	52.296	37.07	21	317 ± 19	345 ± 17	73	12.3 ± 0.1	1.23	1.25	0.01
96Z-61	16	1292	26.519	18.30	15	309 ± 18	311 ± 16	85	12.6 ± 0.1	0.93	1.39	0.01
96Z-65	25	2537	27.653	22.05	19	317 ± 14	320 ± 15	74	11.2 ± 0.2	1.70	1.43	0.01
96Z-101	7	682	24.685	18.02	16	321 ± 28	335 ± 26	16	12.9 ± 0.2	0.77	1.38	0.02
96Z-104	30	757	5.818	2.60	15	458 ± 24	470 ± 23	79	13.1 ± 0.1	0.93	1.48	0.01
96Z-105	29	1483	11.555	5.89	9	427 ± 16	434 ± 15	66	13.0 ± 0.2	1.25	1.44	0.01
96Z-106	32	2114	21.104	11.33	10	388 ± 12	397 ± 12	89	12.6 ± 0.1	1.11	1.42	0.01
96Z-109	24	1138	8.725	5.31	17	348 ± 19	358 ± 18	67	12.8 ± 0.1	0.88	1.31	0.01
96Z-110	21	1260	20.973	11.24	13	385 ± 19	396 ± 17	86	12.3 ± 0.1	1.15	1.45	0.01
96Z-111	20	3850	50.578	28.53	5	360 ± 10	361 ± 9	85	12.1 ± 0.1	1.25	1.59	0.01

Table 1. AFT Summary Table. [a]N_s - number of spontaneous tracks counted. [b]ρ_s – spontaneous track density. [c]^{238}U – average uranium concentration. [d]N_L – number of confined track lengths (TINTs) measured. [e]MTL – mean confined track length and SE – standard error. [f]SD – standard deviation of the track length distribution. [g]D_{par} – long axis of track etch pit. [h]Cl – average chlorine concentration measured by electron microprobe. Apatite grains were mounted on glass slides in epoxy resin, polished to expose prismatic internal apatite surfaces and spontaneous tracks revealed by etching in 5N $HN0_3$ at 20 °C for 20 seconds. Automated counting of fission tracks, with a subsequent manual filtering and correction of track counts as necessary, was carried out in *FastTracks* following autonomous capture of the digital image sets in the partner software, *TrackWorks* [*Gleadow et al.*, 2009]. *FastTracks* was also used to manually measure true confined track lengths, using a refractive index of 1.634 for apatite, as well as automatically measuring their orientation with respect to the crystallographic c-axis direction. The uranium concentrations were measured by LA-ICP-MS [*Hasebe et al.*, 2004] and calibrated against NIST 612 standard glass with Mud Tank Carbonatite apatite as a secondary reference standard. NIST 614 standard glass and

Durango apatite were included at the beginning and end of the analytical sequence as quality controls. Reduction of the LA-ICP-MS data was carried out using the software *Iolite* [*Paton et al.*, 2011]. Single apatite fission track ages were calculated using an absolute calibration based on primary constants (aggregate $\xi = 2.176 \times 10^{-3}$). Pooled ages were calculated according to Hasebe et al. [2004]. Central ages, as well as dispersion, were calculated using the *RadialPlotter* program [*Vermeesch*, 2009].

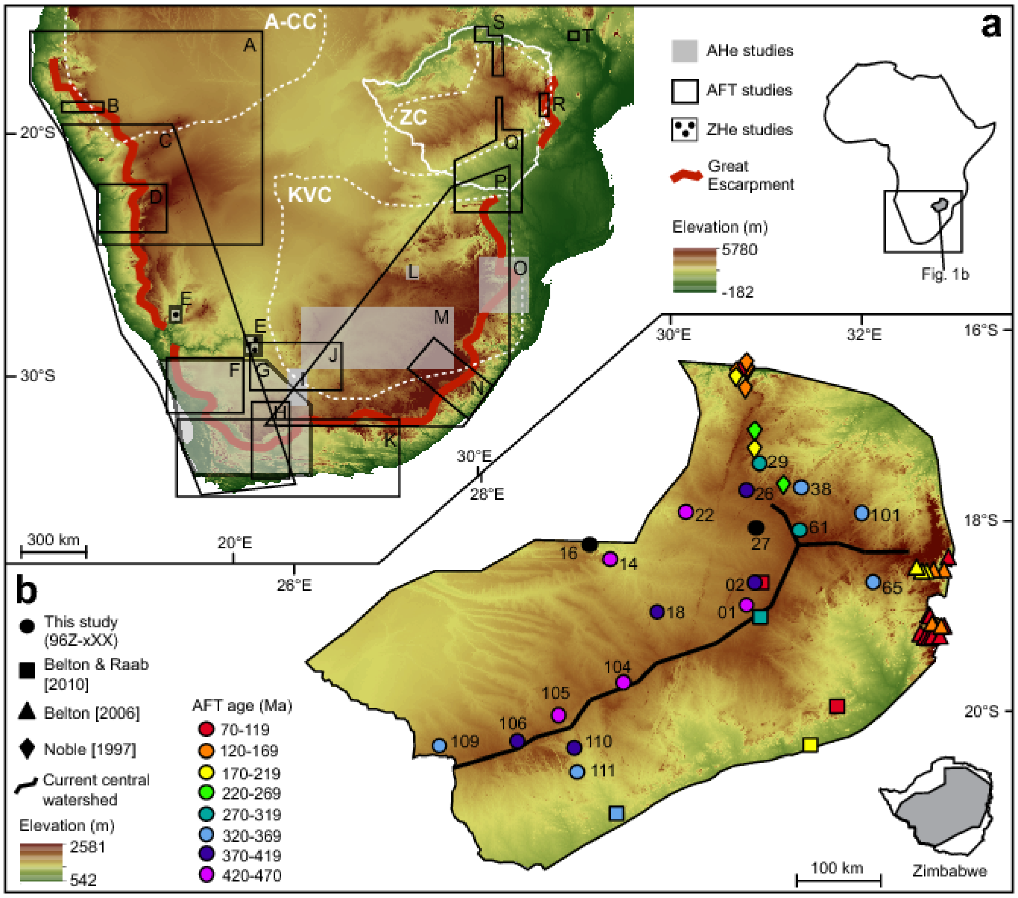

Figure 1. (a) DEM of the southern African plateau showing the Zimbabwe Craton (ZC), Kaapvaal Craton (KVC) and Angola-Congo Cratons (A-CC) (dotted white outlines) as well as the locations of previous apatite (U-Th)/He (AHe), apatite fission track (AFT), and zircon (U-Th)/He (ZHe) studies. Only one other study has utilized the potentially broader temperature sensitivity range of the ZHe system. (A) *Haack* [1983]; *Raab et al.* [2002, 2005]; *Brown et al.* [2014]. (B) *Luft et al.* [2005]. (C) *Brown et al.* [1990]; *Gallagher and Brown* [1999]. (D) [*Cockburn et al.* [2000]. (E) *Kounov et al.* [2013]. (F) *Kounov et al.* [2008, 2009]. (G) *Wildman et al.* [2015, 2016]. (H) *Tinker et al.* [2008]. (I) *Stanley et al.* [2013]. (J) *Wildman et al.* [2017]. (K) *Green et al.* [2015]. (L) *Beucher et al.* [2013]. (M) *Stanley et al.* [2015]. (N) *Brown et al.* [2002]. (O) *Flowers and Schoene* [2010]. (P) *Brown* [1992]. (Q) *Belton and Raab* [2010]. (R) *Belton* [2006]. (S) *Noble* [1997]. (T) *Fernandes et al.* [2015]. Adapted from *Stanley et al.* [2015] and *Artemieva and Vinnik* [2016]. **(b)** DEM of the cratonic region of Zimbabwe with sample localities of available AFT data from this study and previous work. The symbol color and shape represent the apparent AFT age and the study,

respectively. Sample numbers (96Z-xXX) for this study are shown beside each circle. Those samples from this study without AFT ages are colored black.

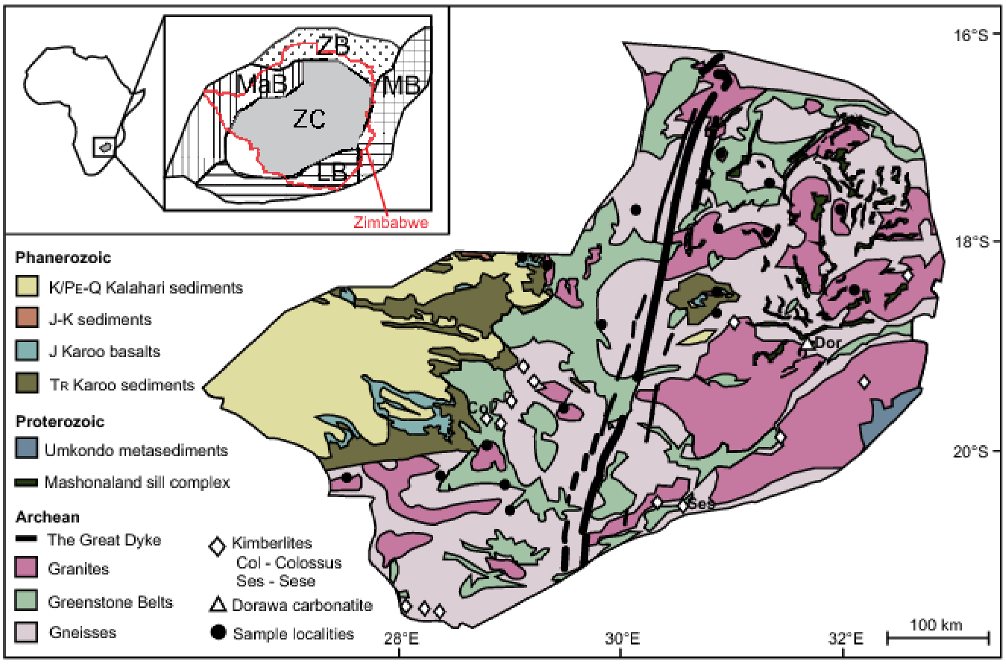

Figure 2. Simplified geological map of the cratonic study area of Zimbabwe based on the 1:1,000,000 geological map of *Stagman* [1977]. Kimberlite and carbonatite locations and names after *Jelsma et al.* [2004, 2009] and *Moore et al.* [2012]. Inset: Tectonic elements that make up Zimbabwe (outlined in red). Zimbabwe is comprised of an Archean cratonic nucleus, the Zimbabwe Craton (ZC), and part of the surrounding late Archean to Early Cambrian mobile belts - Zambezi Belt (ZB), Mozambique Belt (MB), Limpopo Belt (LB) and Magondi Belt (MaB). Adapted from *Kröner* [1977] and *Artemieva and Vinnik* [2016].

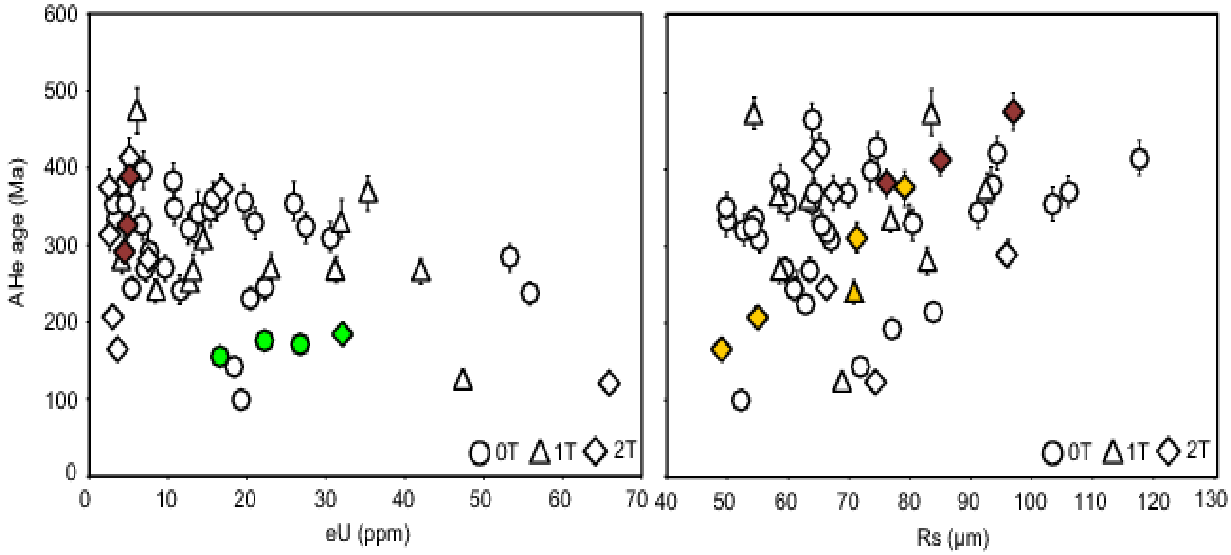

Figure 3. AHe age as a function of effective uranium concentration (eU) (left) and equivalent spherical radius (Rs) (right). AHe ages plotted with 6.2% analytical uncertainty (1σ) bars. For each single grain age, the symbol shape indicates the grain morphology (0T – no terminations, 1T – one termination, 2T – both terminations). The colors refer to samples - 96Z-14 (red), 96Z-38 (green) and 96Z-104 (yellow) - discussed in the text that do exhibit a positive AHe age-eU or -Rs correlation. For a similar figure with all samples individually identified, see Figure S4.

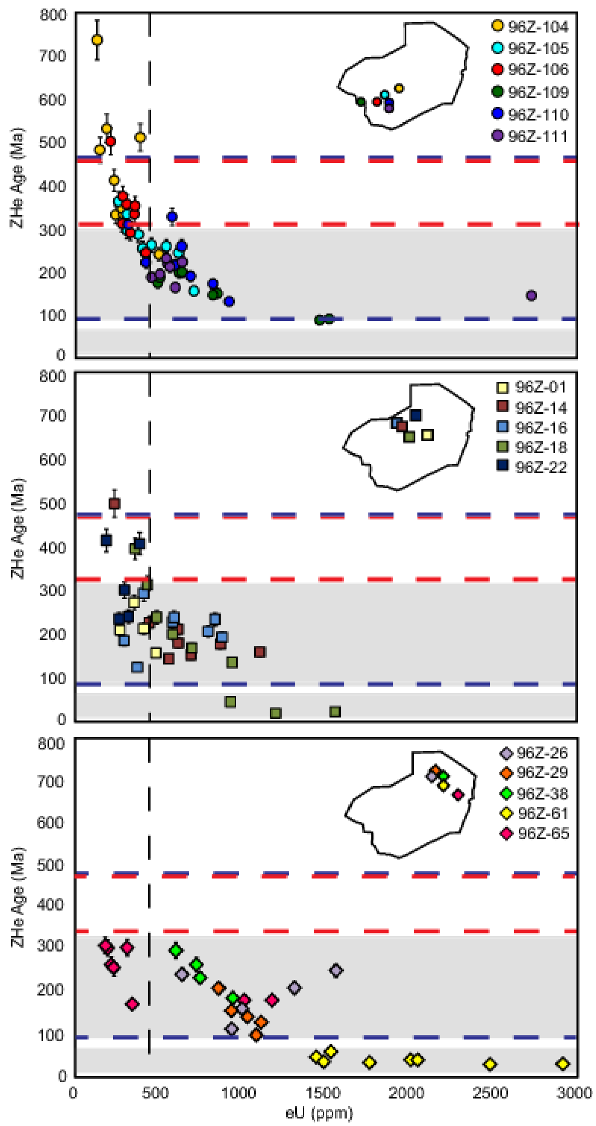

Figure 4. ZHe age as a function of eU for samples from the southwest (upper panel), central (middle panel) and northeastern (lower panel) regions of the Zimbabwe Craton. ZHe ages plotted with 6.2% analytical uncertainty (1σ) bars. Sample localities shown on craton map (top right of each panel). Grey boxes indicate two apparent significant ZHe age bands. The black dashed line represents the upper limit of the eU zone with the most drastic ZHe-eU correlation. The blue and red dashed lines delimit the AHe and AFT age ranges, respectively. It is important to note that the upper and lower ZHe age bands are younger than the AFT and AHe age ranges, respectively.

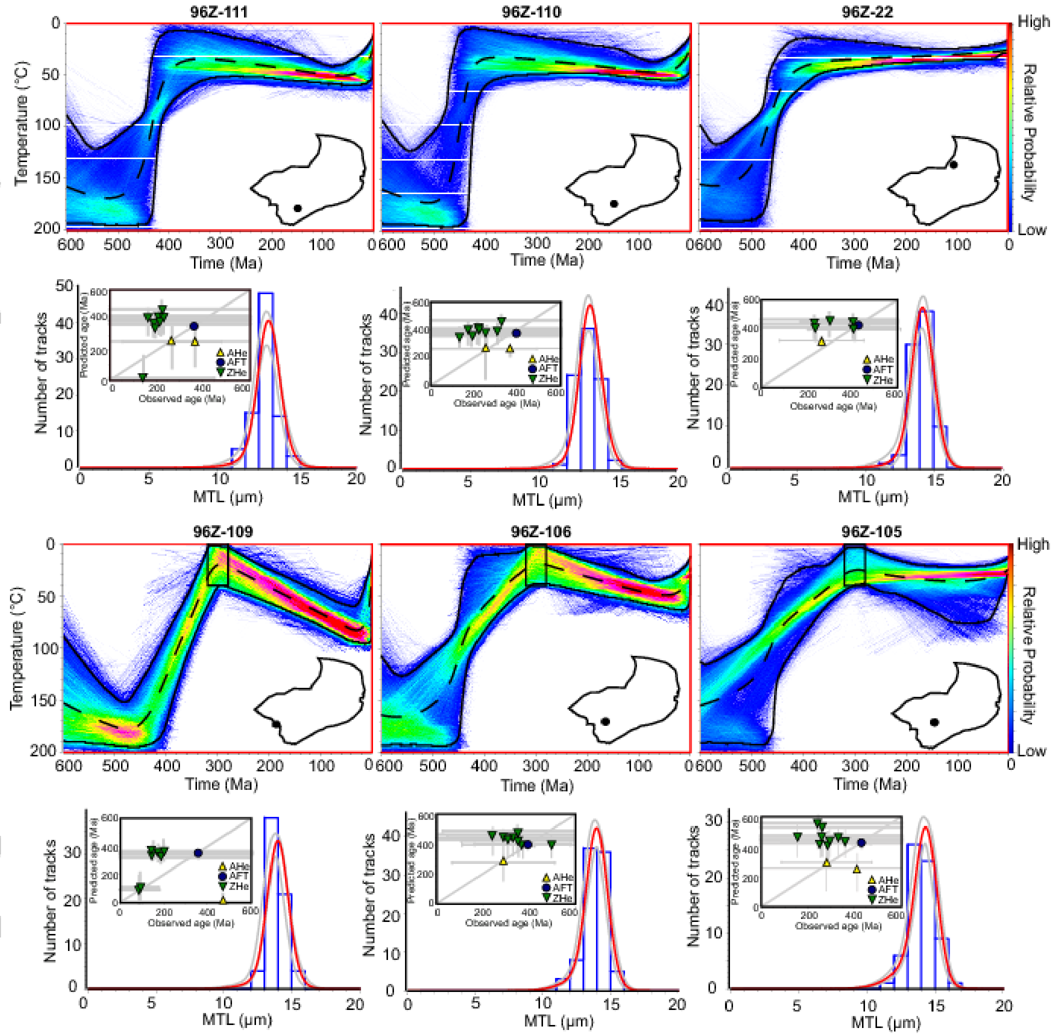

Figure 5. Thermal history models of representative samples from across the Zimbabwe Craton showing the ~500 Ma initiation of more rapid cooling. Thermal histories for 96Z-111, -110, and -22 show moderately rapid cooling between ~500-430 Ma whereas samples 96Z-109, -106, and -105 experienced more protracted cooling until initiation of Karoo sedimentation (~300 Ma). Figure elements of upper panel: The color map represents the posterior probability distribution of accepted thermal history models with the dashed line representing the (weighted mean) expected model and the black solid lines representing the 95% confidence intervals. The red box represents the prior time-temperature model space and the black boxes represent additional thermal history constraints discussed in Section 4.1. Figure elements of lower panel: The histogram represents the observed MTL distribution, the red curve represents the predicted distribution and grey lines show the 95% confidence

intervals of the predicted distribution. Inset in lower panel shows the observed ages (with resampled He error values) plotted against the predicted ages.

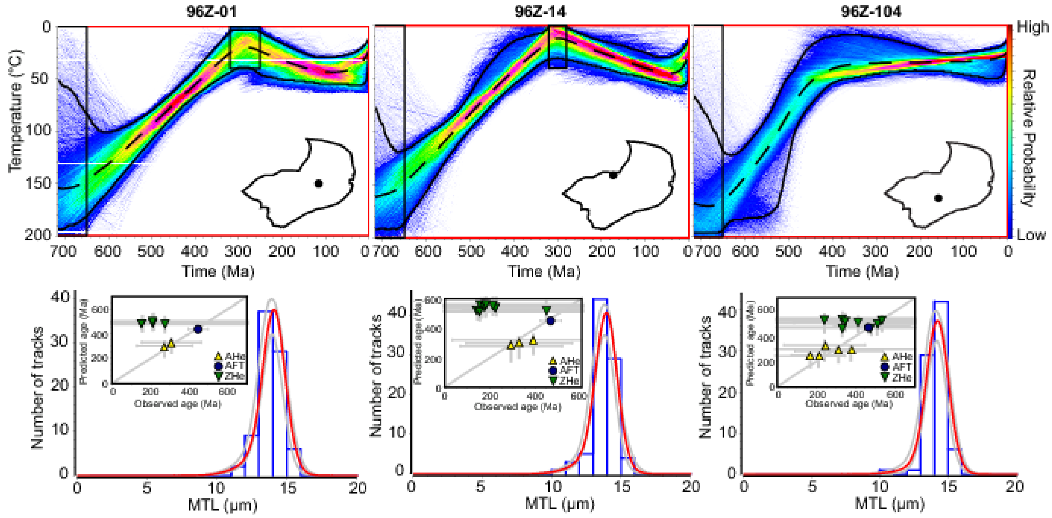

Figure 6. Thermal history models (upper panel) for three samples from the central region of the Zimbabwe Craton showing protracted cooling from the Cryogenian (~680 Ma) until the initiation of Karoo sedimentation (~300 Ma). Model predictions are shown in the lower panel. See Figure 5 for a description of figure elements.

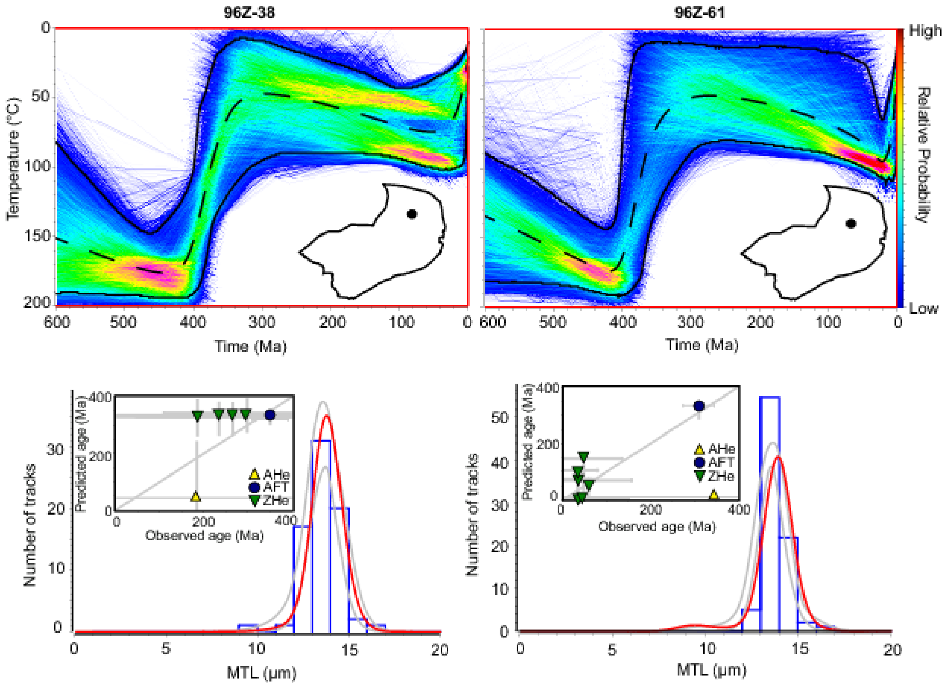

Figure 7. Thermal history models for two samples from the northeastern region of the Zimbabwe Craton that show rapid cooling between ~415-335 Ma (upper panel) and their model predictions (lower panel). See Figure 5 for a description of figure elements.

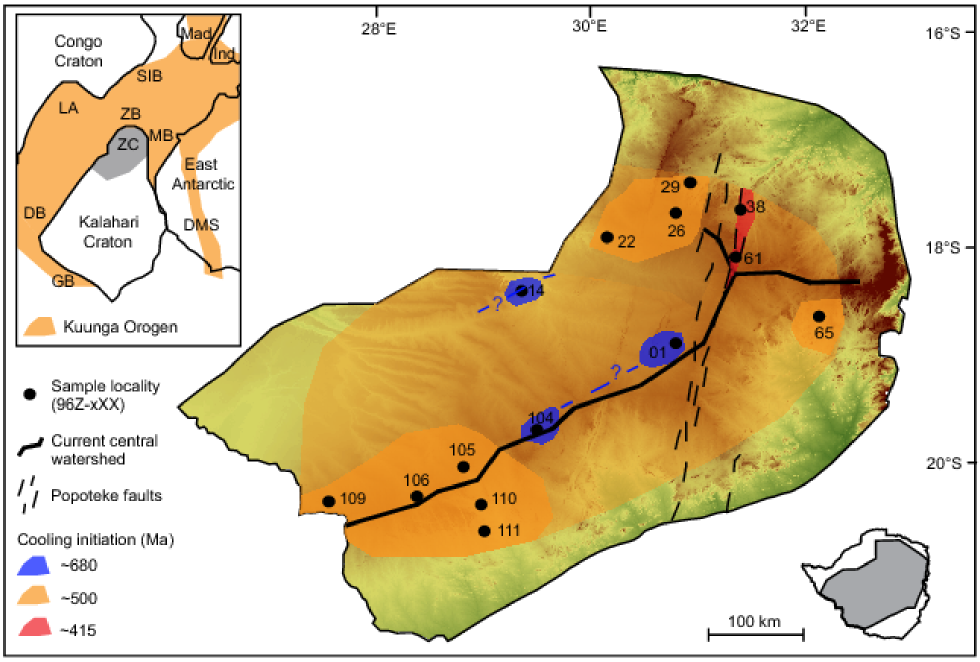

Figure 8. Map of the study area showing the spatial pattern of the late Neoproterozoic to middle Paleozoic cooling onsets (bold colored regions) derived from the thermal history models (Figs. 5, 6, 7 and S7) of the numbered samples. Samples from across the current broad topographic high underwent substantial cooling during this time. The semi-transparent orange area represents the inferred initiation of cooling based on the widespread occurrence of the ~500 Ma cooling onset. Location of Popoteke faults after *Wilson* [1990]. Inset shows the Cambrian configuration of central Gondwana illustrating the adjacent Pan-African mobile belts (GB: Gariep Belt, DB: Damara Belt, DMS: Dronning Maud Suture, LA: Lufilian Arc, ZB: Zambezi Belt, MB: Mozambique Belt, SIB: Southern Irumide Belt) surrounding the Zimbabwe Craton (ZC) that formed as a result of the Kuunga Orogeny. Adapted from *Meert* [2002], *Collins and Pisarevsky* [2005] and *Goscombe and Gray* [2008]. See Figure 1b for DEM legend.

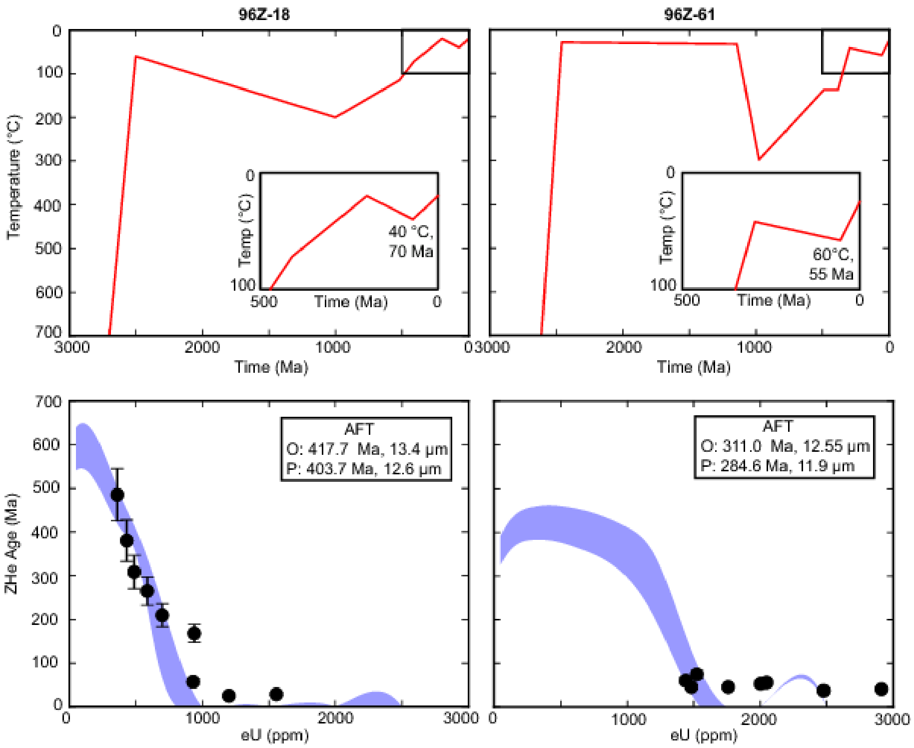

Figure 9. Thermal history forward models for two samples with extremely damaged (high eU) zircon grains. Upper panel: Forward thermal history model with inset showing an enlargement of the 500 Ma to 0 Ma thermal history and onset of most recent cooling labelled. Lower panel: Forward model predictions. Black spots represent observed ZHe ages as a function of eU. Blue curve represents the predicted ZHe age-eU trend with 2σ envelope. Observed (O) and predicted (P) AFT data also included.